

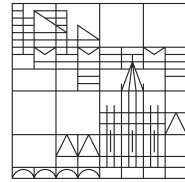
# **Electronic Transport through Superconducting Atomic Contacts under Microwave Irradiation**

**Master's thesis**

submitted by  
**Raif, Patrick**

at the

Universität  
Konstanz



Faculty of Science  
Department of Physics

1. Reviewer: Prof. Dr. Elke Scheer  
Department of Physics, Mesoscopic Systems  
Universität Konstanz

2. Reviewer: Prof. Dr. Sebastian T. B. Gönnenwein  
Department of Physics, Modern Materials Science  
Universität Konstanz

Konstanz, 2024



## Abstract

In this master's thesis, two different types of microwave irradiation were installed in a milli-Kelvin cryostat and characterized by means of microwave effects on superconducting atomic contacts. In addition to the initially expected SHAPIRO steps, further steps were observed in the *IV*-characteristics. The photon-assisted tunneling (PAT) can be fully understood within the framework of the TIEN-GORDON model. For effects of microwaves on higher order transport processes (PAMAR) the model has to be extended as the comparison of the measurement data and a simulation based on the simple TIEN-GORDON model reveals. A closer look at the SHAPIRO steps shows that they are not described by the equation expected from theory, but also by a modified expression of the TIEN-GORDON equation. The fractional SHAPIRO steps, which become visible in atomic contacts with high transmission channels at high frequencies and which are no SHAPIRO steps in the original sense, thus represent a new observation.

## Zusammenfassung

In dieser Masterarbeit wurden zwei Arten von Mikrowellenbestrahlung in einem Milli-Kelvin-Kryostaten installiert und anhand von Mikrowelleneffekten supraleitender atomarer Kontakte charakterisiert. Zusätzlich zu den ursprünglich erwarteten SHAPIRO-Stufen wurden weitere Stufen in den *IV*-Kennlinien beobachtet. Das Photon-Assisted Tunneling (PAT) kann im Rahmen des TIEN-GORDON-Modells vollständig verstanden werden. Für Effekte von Mikrowellen auf elektronische Transportprozesse höherer Ordnung (PAMAR) muss das Modell erweitert werden, was durch den Vergleich der Messdaten mit einer Simulation auf der Basis des einfachen TIEN-GORDON-Modells zeigt. Eine genauere Betrachtung der SHAPIRO-Stufen zeigt, dass sie nicht durch die aus der Theorie erwartete Gleichung, sondern ebenfalls durch eine modifizierte TIEN-GORDON-Gleichung beschrieben werden. Die fraktionierten SHAPIRO-Stufen, die bei atomaren Kontakten mit hoher Transmission bei hohen Frequenzen sichtbar werden und keine echten SHAPIRO-Stufen im eigentlichen Sinne sind, stellen somit eine neue Beobachtung dar.



# Contents

<b>1</b>	<b>Introduction</b>	<b>1</b>
<b>2</b>	<b>Theoretical Background</b>	<b>3</b>
2.1	Superconductivity . . . . .	3
2.2	Tunneling in Superconductors . . . . .	4
2.3	Mesoscopic Transport . . . . .	5
2.4	(Multiple) Andreev Reflections . . . . .	6
2.5	Josephson Effect . . . . .	7
2.6	Shapiro Steps . . . . .	9
2.7	Photo-Assisted Tunneling . . . . .	11
2.8	State of the Art of Research . . . . .	13
<b>3</b>	<b>Setup and Samples</b>	<b>17</b>
3.1	Cryogenics and Mechanics . . . . .	17
3.2	Electronics . . . . .	18
3.3	Microwave Irradiation . . . . .	19
3.4	Sample Fabrication . . . . .	21
<b>4</b>	<b>Measurements and Results</b>	<b>23</b>
4.1	Low-Ohmic Contacts . . . . .	23
4.2	Atomic Contacts under Microwave Irradiation . . . . .	28
4.2.1	Tunnel Contact . . . . .	30
4.2.2	Atomic Contact with Low Transmission . . . . .	35
4.2.3	Atomic Contact with High Transmission . . . . .	38
4.2.4	Atomic Contact with Perfect Transmission . . . . .	44
4.2.5	Closed Contact with High Conductance . . . . .	44
4.2.6	Comparison of Antenna and stripline . . . . .	49
<b>5</b>	<b>Conclusion and Outlook</b>	<b>51</b>
<b>6</b>	<b>Appendix</b>	<b>53</b>
6.1	Microwave Effects on Low-Ohmic Contacts . . . . .	54
6.2	Atomic Contacts in Magnetic Field . . . . .	54
6.3	Simulation based on a theoretical curve . . . . .	56
<b>References</b>		<b>61</b>



## 1 Introduction

Since the single-electron transistor (SET) was proposed by AVERIN and LIKHAREV in 1985 [1], there have been many experiments with different realizations of this device, especially in the 1990s. An SET is by weakly coupling a small metallic island to two electrodes via tunnel junctions. The transistor-like behavior can be explained by the effect of COULOMB blockade, where the electronic transport is suppressed for low bias voltages and that can be controlled by a gate electrode. This blocking effect is due to the charging energy  $E_C = e^2/2C$  with the electrons charge  $e$  and the capacitance  $C$  of the island, which corresponds to the energy required to add or remove an electron from the island.

There has been steady progress in the understanding of SETs. Current research shows, for example how Coulomb oscillations vanish when the charge fluctuations increase as a consequence of a junction with almost perfect transmission [2] and how Coulomb blockade and multiple ANDREEV reflections (MAR) interact [3–5].

A special expertise of the SCHEER group are mechanically controllable break junctions (MCBJ), which allow to adjust the sample resistance *in situ*. This technique requires a flexible substrate and a bending mechanism as shown in figure 1.1a. MCBJs are able to form an atomic contacts with a small numbers of channels and with variable transmissions that can give rise to higher order transport processes in superconductors called multiple ANDREEV reflections (MAR). By replacing one of the two tunnel junctions of the SET, usually formed by an aluminum oxide barrier, with a MCBJ, it was possible to create a very versatile MCBJ-SET. A scanning electron microscope (SEM) image of this MCBJ-SET is presented in figure 1.1b.

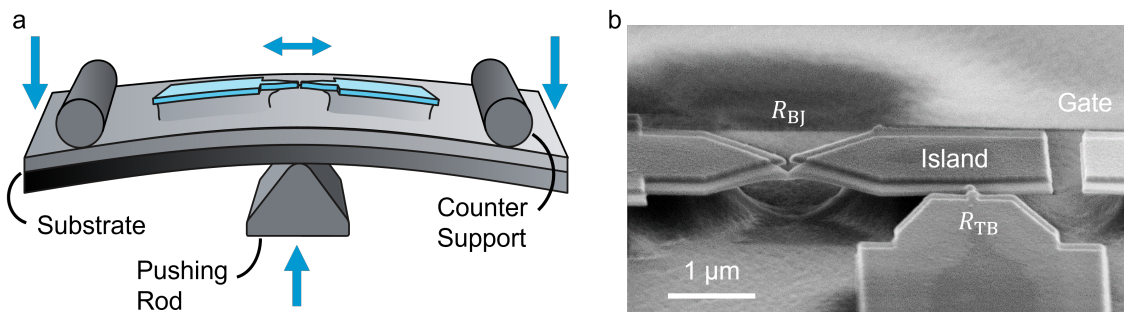


**Figure 1.1:** A schematics of the three-point bending mechanism for a MCBJ-SET is shown in (a), and an SEM image of the MCBJ-SET in (b).

While previous experiments on all-superconducting MCBJ-SETs tried to attenuate high frequencies as much as possible [6], next step of this research project, which is continued within the scope of the Collaborative Research Center SFB 1432 is to irradiate this type of device with microwaves to perturb the system in a controlled manner. In this way, the interplay between quantum fluctuations of the charge and the strong non-equilibrium created by irradiation is to be investigated.

The idea of this master's thesis project is to set up the microwave irradiation and characterize it by performing some first measurements on a simpler system before

returning to the MCBJ-SET. For this purpose, we installed two coaxial cables to couple two different microwave emitters, namely an antenna and a stripline, to our sample and test them against each other. A basic aluminum MCBJ is an interesting simplification of the all-superconducting MCBJ-SET. Since aluminum is a superconductor, the atomic contacts as formed in a MCBJ can be understood as JOSEPHSON junctions. Under microwave irradiation they are known to exhibit replicas of the supercurrent branch which are called SHAPIRO steps.

We expected to see SHAPIRO steps (showing up as peaks in a  $dI/dV$ -curve) but found many more peaks in addition to those at the positions expected for the SHAPIRO steps. The additional features could be attributed to photon-assisted tunneling (PAT) of quasi-particles at the edges of the superconductor's energy gap and understood within the framework of the well known TIEN-GORDON model. Some atomic contacts with intermediate and high transmissions even showed photo-assisted tunneling on the MARs (PAMAR), that go beyond the simple TIEN-GORDON model. For high frequencies and high conductance we observe half-integer SHAPIRO steps show up as additional peaks in between the integer SHAPIRO steps. These fractional SHAPIRO steps originate from a non-sinusoidal current-phase relation have already been reported to literature as well as the PAMAR. Upon closer examination of the amplitude of the SHAPIRO steps, it is striking that not the equation for SHAPIRO steps, but by an expression that is similar to the TIEN-GORDON equation describes our data. Following previous work on comparable systems, the replicas of the supercurrent therefore have to be understood in terms of phase-incoherent tunneling of COOPER pairs rather than SHAPIRO steps. In this sense, the fractional "SHAPIRO steps" are a new observation.

Before discussing the interesting effects of microwave irradiation on atomic contacts, I will present some theoretical foundations as a prerequisite to a brief review of well-known and up-to-date literature. Next, I will describe our setup and samples, in particular their characterization using a magnetic field before the MCBJ is opened for the first time to form an atomic contact. The main focus of this work lies on measurements with microwave irradiation of different frequency and power. In order to maintain an overview of the rich microwave effects, I will begin with the discussion of a tunnel contact, since only PAT occurs here. Subsequently, I will discuss atomic contacts with increasing transmissions and conclude the discussion of the measurement results with a comparison of antenna and stripline.

In the appendix I show some additional measurements that complete the characterization of our samples, but are not directly related to the electronic transport through superconducting atomic contacts under microwave irradiation.

## 2 Theoretical Background

This chapter is intended to provide a brief insight into the theoretical fundamentals necessary to understand the discussion of the measurements on superconducting atomic contacts under microwave irradiation. In this regard, I assume a basic knowledge of superconductivity, which can be found in any text book on solid state physics. For a more in-depth introduction to the topic of superconductivity, the textbook of TINKHAM [7] is particularly recommended.

### 2.1 Superconductivity

Despite assuming some basic knowledge, I would like to mention a few basic properties of superconductors, that are important for the characterization of the measured samples. Every superconductor has a critical temperature  $T_c$ , a critical magnetic field  $B_c$ , and a critical current  $I_c$ , which are material and geometry dependent. Once a superconductor exceeds these critical values, it loses its superconducting properties and transitions to its resistive normal conducting phase. Thin films of superconductors are known to have increased critical magnetic field  $B_c$ . Very thin films of aluminum also show an enhanced critical temperature  $T_c$ . The critical current  $I_c$  depends especially on the cross-section of the conductor. For films of  $\sim 1\text{ }\mu\text{m}$  we reach the bulk limit which corresponds to a critical magnetic field of  $B_C = 10\text{ mT}$  in the case of aluminum. Thin aluminum films of less than 100 nm can show enhanced critical magnetic fields of  $B_c \approx 100\text{ mT}$  or even  $B_c > 1\text{ T}$  for films of less than 10 nm thickness [8]. The increase in critical temperature  $T_c$  for aluminum is more subtle with only slightly elevated critical temperature  $T_c$  for a film thickness of  $\sim 100\text{ nm}$  compared to the value for bulk material ( $T_{C,\text{bulk}} = 1.19\text{ K}$ ) and values of  $\sim 2\text{ K}$  for films thinner than 10 nm [9]. The critical temperature of the sample we have been primarily measuring was determined by OLIVER IRLENKAUF during a warm-up measurement to be approximately  $T_c = 1.2\text{ K}$ . This value is very close to the value of bulk aluminum, which is within the range of what is expected for a sample with a thickness of 80 nm.

One important finding of the microscopic description of superconductivity developed by BARDEEN, COOPER and SCHRIEFFER (BCS theory) is the dependence of the energy gap  $\Delta$  for quasi-particle excitations, on the critical temperature  $T_c$

$$\Delta(T = 0) = 1.764 \cdot k_B \cdot T_c \quad (2.1)$$

with the BOLTZMANN constant  $k_B \approx 1.38 \times 10^{-23}\text{ J/K}$ . For temperatures below half the critical temperature, the energy gap  $\Delta$  is mostly independent of the temperature

$$\frac{\Delta(T)}{\Delta(0)} \approx 1.74 \cdot \sqrt{1 - \frac{T}{T_c}} \quad (2.2)$$

as the square root term flattens out for low temperatures [7]. The energy gap for our aluminum sample was determined by OLIVER IRLENKAUF via fitting a tunnel

contact. The best fit could be achieved with  $\Delta = 188 \mu\text{eV}$  assuming no gap asymmetry for the two electrodes of the MCBJ. All subsequent calculations and fits are based on this value for the gap energy. Taking equation 2.1 to estimate the gap energy and  $T_c = 1.2 \text{ K}$  from above we obtain  $\Delta = 182 \mu\text{eV}$  which is close to the value determined by fitting the measurements on a tunnel contact.

The density of states  $\text{DOS}_S(E)$  for quasi-particle excitations is zero for energies smaller than the energy gap  $\Delta$  and

$$\text{DOS}_S(E) = \text{DOS}_N(0) \cdot \frac{E}{\sqrt{E^2 - \Delta^2}} \quad (2.3)$$

for energies above the energy gap  $\Delta$  where  $\text{DOS}_N(0)$  is the density of states in the normal conducting state, which is approximately constant close to the FERMI energy. A sketch of the density of states for a superconductor at finite temperature can be found in figure 2.1 which shows the quasi-particle tunneling in superconductors.

## 2.2 Tunneling in Superconductors

To discuss the quasi-particle tunneling between superconductors, one usually uses the semiconductor model with electron-like and hole-like quasi-particle excitations for energies above and below the FERMI energy  $\mu$ . Tunneling from one superconductor to the other is only possible if there are unoccupied states available. This condition can be achieved by applying a sufficiently large bias voltage and is facilitated by finite temperatures. For  $T > 0$ , there are thermal excitations as shown in figure 2.1 which allow for tunneling below the threshold of  $eV < \Delta_1 + \Delta_2$ , which is absent for  $T = 0$ .

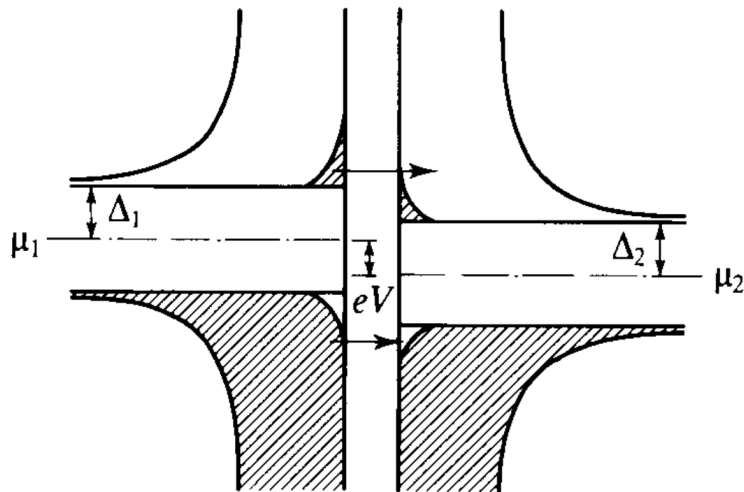


**Figure 2.1:** Schematics of a superconductor-superconductor tunnel contact showing the density of states for both superconductors at  $T > 0$  which allows for tunneling of thermally excited quasi-particles below the threshold of  $eV < \Delta_1 + \Delta_2$ . The figure was taken from TINKHAM [7].

The tunnel current between two superconductors can be calculated numerically by integrating the following expression

$$I_{S-S} = \frac{G_{N-N}}{e} \int_{-\infty}^{\infty} \frac{|E|}{\sqrt{E^2 - \Delta_1^2}} \frac{|E + eV|}{\sqrt{(E + eV)^2 - \Delta_2^2}} [f(E) - f(E + eV)] dE \quad (2.4)$$

with the normal conductance  $G_{N-N} = 1/R$ , the energy gaps  $\Delta_1$  and  $\Delta_2$ , and the FERMI distribution  $f(E)$ . The result is presented in figure 2.2 as current-voltage ( $IV$ ) curve for zero and finite temperature. At  $T = 0$  there is no current flow as long as  $eV < \Delta_1 + \Delta_2$ . Above  $\Delta_1 + \Delta_2$  the current suddenly jumps to a finite value and increases further with the bias voltage. For  $T > 0$  the rise of the tunneling current at  $\Delta_1 + \Delta_2$  is thermally rounded and there is a peak at  $|\Delta_1 - \Delta_2|$ . If the gaps of the two superconductors are identical, there is a logarithmic singularity resulting in a tunnel current at zero bias. These sharp features are well suited to determine the gap of a superconductor as first performed by GIAEVER in 1960 [10].

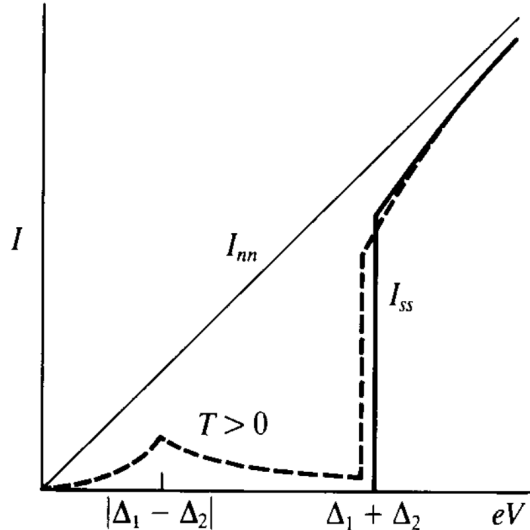


**Figure 2.2:** Current-voltage characteristics of a superconductor-superconductor tunnel junction for  $T = 0$  (solid line) and  $T > 0$  (dashed line). If the energy gaps are identical, the peak at  $|\Delta_1 - \Delta_2|$  would result in a current at zero bias voltage. The figure was taken from TINKHAM [7].

## 2.3 Mesoscopic Transport

Atomic contacts as formed in a MCBJ behave differently than a macroscopic conductor as the elastic mean free path of the electrons is now greater than the size of the contact. We therefore have to consider a ballistic conductor instead of a diffusive one. To understand the electronic transport in this regime, one has to think of reservoirs of electrons that can only travel from one side of the junction to the other if there is an unoccupied state available. This leads to the formation of so called conduction

channels which have a maximum conductance of

$$G_0 = \frac{2e^2}{h} \quad (2.5)$$

with the elementary charge  $e$  and the PLANCK constant  $h$ . The factor of 2 comes from considering spin degeneracy.  $G_0$  is commonly known as the conductance quantum. The total conductance  $G$  of an atomic contact is simply the sum over the contributions of all conduction channels with transmissions  $\tau_i$  multiplied by the conductance quantum  $G_0$

$$G = G_0 \sum_i \tau_i \quad (2.6)$$

with values for the transmissions  $\tau_i$  being numbers between 0 and 1, which describes the transmission probability of an electron through a conduction channel. The equation 2.6 is also known as LANDAUER formula [11]. For a detailed discussion of mesoscopic transport, see reference [12].

A peculiarity of the atomic contacts made from aluminum we study is that every atom can contribute with up to three conduction channels to the electric transport as aluminum has three valence electrons. Even for contacts with a conductance of less than one conductance quantum, at least two channels have been found to contribute to the transport [13]. Figure 2.3 shows the total transmission (which corresponds to the total conductance) in the opening trace of an aluminum MCBJ together with the individual transmissions of the contributing channels. The transmission of a channel typically rises before a rearrangement of the conduction channels takes place. (Almost) perfect transmission channels can be achieved more easily for a total conductance greater than  $G > 2G_0$ .

## 2.4 (Multiple) Andreev Reflections

Other than a tunnel contact as shown in figure 2.2 and discussed above, atomic contacts with higher transmissions show a rich subgap structure, that cannot be explained by single-particle tunneling. Figure 2.4 shows  $IV$ -curves that have been calculated by CUEVAS *et al.* [14] for one superconducting channel at  $T = 0$  for different transmissions. Experimental data can resemble these theoretical curves very well but show some rounding of the kinks at the voltages  $V = \Delta/me$  due to finite temperature and deviations from the ideal BCS density of states. However, the leading channel, meaning the one with the highest transmission, determines the overall shape of the  $IV$ -curve and it is possible to decompose a contact into the number of individual channels and their transmissions that contribute to transport. This set of transmissions is often referred to as the PIN code of a junction.

To understand the  $IV$ -curves for a superconducting contact one has to introduce the phenomenon of (multiple) ANDREEV reflections. At  $T = 0$  electronic transport is only possible for bias voltages above the threshold  $eV > 2\Delta$  assuming no gap asymmetry when only one particle is involved. This is shown in figure 2.5a. For bias voltages above  $eV > \Delta$  we can transport an electron across the tunnel barrier if there is a hole of the appropriate energy simultaneously reflected in the opposite direction. This

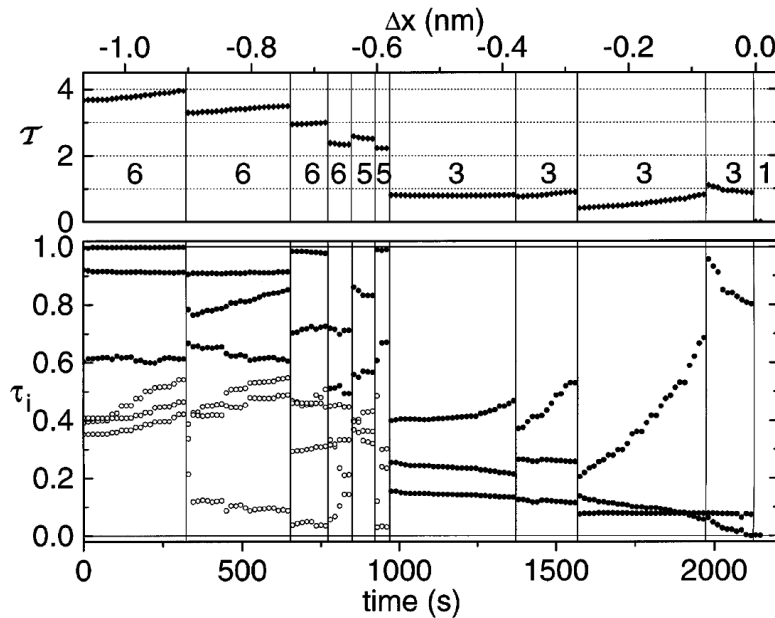


**Figure 2.3:** Opening trace of an aluminum MCBJ showing the evolution of the total transmission as well as the transmissions of the individual contributing channels that have been obtained by fitting  $IV$ -curves measured while opening the MCBJ. The figure was taken from SCHEER *et al.* [13].

process is called ANDREEV reflection and transports two charges across the tunnel barrier. The probability for this process is therefore  $\tau^2$  as two particles have to be transmitted at the same time. A schematic of the ANDREEV reflection is presented in 2.5b. Analogous to the two-particle process there are higher-order processes where  $n$  particles are involved in the transport. The onset of these so called multiple ANDREEV reflections (MAR) happens at  $eV > 2\Delta/m$  with  $m$  being the order of the MAR. The probability of the higher-order processes and therefore their contribution to the total current decreases for increasing order as  $\tau^n$ . The threshold voltages and their contribution to the total current is shown in figure 2.5d, the schematics above in figure 2.5c shows MAR of order  $m = 3$ .

## 2.5 Josephson Effect

In 1962, JOSEPHSON predicted the tunneling of COOPER pairs at zero voltage [16]. Junctions of two superconducting electrodes separated by a thin barrier are therefore called JOSEPHSON junctions. A barrier can be an insulator as originally proposed by JOSEPHSON, a normal metal, a ferromagnet or a narrow constriction. There are two famous JOSEPHSON relations, the derivation of which can be found in [17], for example. The lecture notes of GROSS and MARX on their lecture "Applied Superconductivity" also present the derivation very clearly [18]. The first equation relates the supercurrent  $I_S$  to the phase difference of the Ginzburg-Landau wave functions of the two electrodes

$$I_S = I_c \cdot \sin(\varphi) \quad (2.7)$$

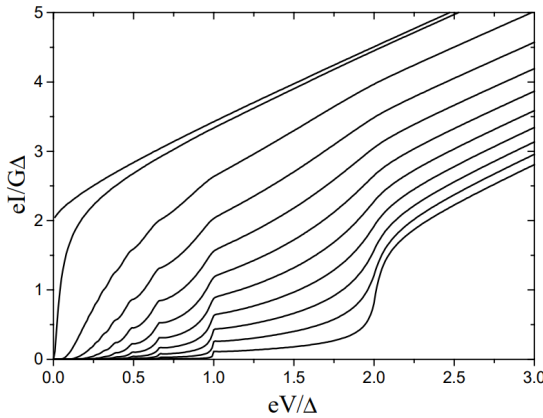


**Figure 2.4:** Calculations for the dc component of the current in a one channel superconducting contact at  $T = 0$ . Current and voltage have been rescaled in units of the energy gap. Higher-order transport processes show up as kinks in the  $IV$ -curve at voltages  $V = \Delta/m e$ . The upper two curves correspond to  $\tau = 1$  and 0.99, the next one is  $\tau = 0.9$  and the following curves decrease by 0.1 each, meaning the lowest curve corresponds to  $\tau = 0.1$ . The figure was taken from AGRAIT *et al.* [15].

where  $I_c$  is the critical current of the junction and  $\varphi$  is the phase difference. In the case of weak coupling, we simply have a sinusoidal current-phase relation. This is no longer the case for very high transmissions, where higher-order transport processes cannot be neglected.

If a constant voltage  $V$  is applied to the JOSEPHSON junction, the second relation simplifies to

$$\frac{\partial \varphi}{\partial t} = \frac{2e}{\hbar} V \quad (2.8)$$

with the elementary charge  $e$  and the reduced PLANCK constant  $\hbar$ . The supercurrent for a constant voltage consequently is given by

$$I_S = I_c \cdot \sin \left( \varphi_0 + \frac{2e}{\hbar} V t \right) \quad (2.9)$$

with the JOSEPHSON frequency  $\omega = 2eV/\hbar$ . The junction effectively acts as voltage biasto-frequency converter, this is called the ac JOSEPHSON effect. As frequencies can be measured easily, the ac JOSEPHSON effect was chosen to redefine the Ampere in the new International System of Units in 2019. The JOSEPHSON voltage standard is  $2e/h = 483\,597\,848\,416\,984$  GHz/V [19].

Further insight into the dynamics of the Josephson junction can be gained by having a look at the Resistively and Capacitively Shunted Junction (RCSJ) model, an introduction to this can be found in the already mentioned sources. I do not want to go into detail here, as I only want to introduce the STEWARD-MCCUMBER [20, 21] parameter  $\beta_C$  which is defined as

$$\beta_C = \frac{2e}{\hbar} I_c R_N^2 C \quad (2.10)$$

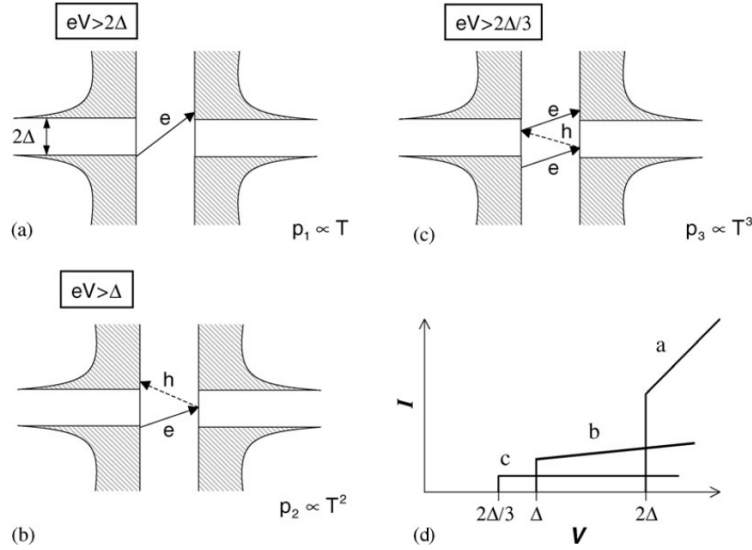


**Figure 2.5:** Schematic to explain the subgap structure in atomic contacts showing (a) quasi-particle tunneling, (b) ANDREEV reflection, (c) MAR of order  $m = 3$  and (d) the corresponding threshold voltages and the contribution of processes (a)-(c) to the total current. The figure was taken from AGRAIT *et al.* [15].

where one calls a junction underdamped for  $\beta_C \gg 1$  and overdamped for  $\beta_C \ll 1$ . Underdamped junctions show a hysteretic switching behavior. For atomic contacts as for the MCBJ in our case, the capacitances are usually small so that the junction is overdamped and therefore non-hysteretic. This can be seen from comparing our measurements to the theory and was also reported by CRON in his doctoral thesis who worked on a similar system [22].

## 2.6 Shapiro Steps

When irradiating a JOSEPHSON junction with microwaves, one can observe plateaus of constant voltage in the  $IV$ -curve. Named after the first who measured them, SHAPIRO steps are basically the manifestation of the inverse ac JOSEPHSON effect. Assuming perfect voltage bias for simplicity, microwave irradiation will cause an alternating voltage  $V_\omega$  at the junction resulting in

$$V(t) = V_0 + V_\omega \cdot \cos(\omega t). \quad (2.11)$$

Using the second JOSEPHSON relation 2.8 we receive by integrating the time dependent voltage

$$\varphi(t) = \varphi_0 + \frac{2eV_0}{\hbar} + \frac{2eV_\omega}{\hbar\omega} \cdot \sin(\omega t). \quad (2.12)$$

By substituting this result into the first JOSEPHSON relation 2.7 and expanding the sine of a sine in terms of BESSEL functions of the first kind, which is shown in detail

in [17, 18], we obtain

$$I_S(V_0, \omega, V_\omega) = I_c \cdot \sum_{n=-\infty}^{\infty} (-1)^n \cdot J_n \left( \frac{2eV_\omega}{\hbar\omega} \right) \cdot \sin \left( \varphi_0 + \frac{2eV_0}{\hbar} - n\omega t \right). \quad (2.13)$$

A dc contribution to the current can only be measured, if the dc voltage has one of the values for SHAPIRO steps

$$V_n = \frac{n\hbar\omega}{2e} \quad (2.14)$$

with integer values for  $n$ . The SHAPIRO steps for an overdamped JOSEPHSON junction are shown in figure 2.6. In the case of ideal voltage bias we have been considering so far, I would rather follow WALDRAM and call the plateaus constant voltage "voltage spikes" instead of voltage steps [23]. The amplitude of the average dc current is given by the absolute value of the BESSEL function as shown in the inset of figure 2.6

$$|I_n| = I_c \cdot \left| J_n \left( \frac{2eV_\omega}{\hbar\omega} \right) \right|. \quad (2.15)$$

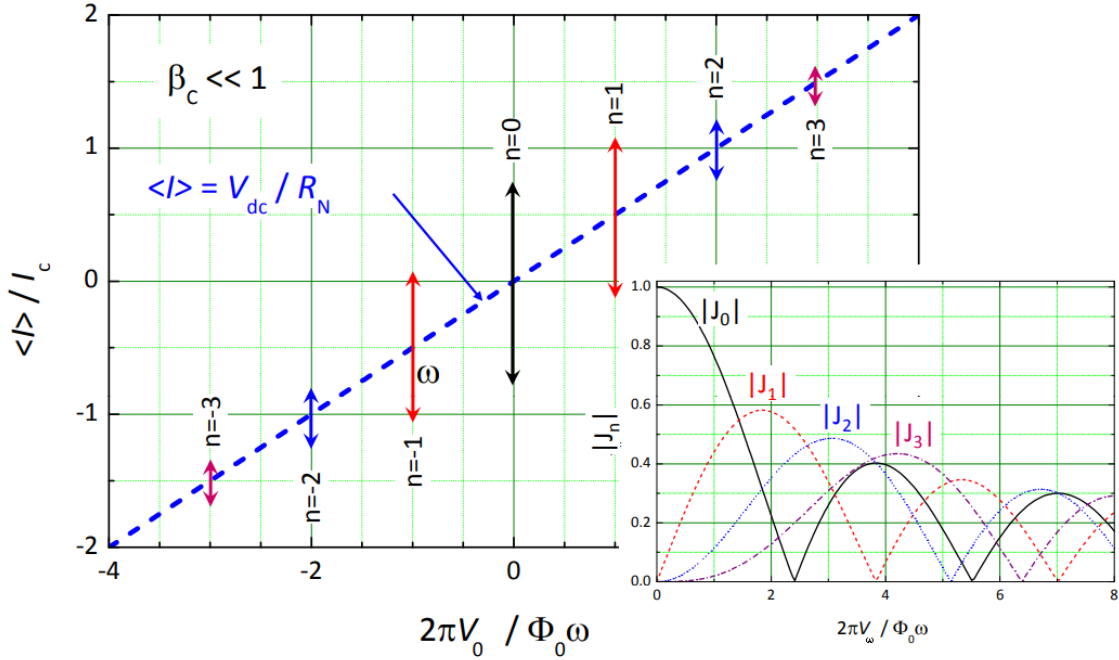


**Figure 2.6:** SHAPIRO spikes show up when plotting the dc component of the current against the bias voltage  $V_0$  if the junction is irradiated with microwaves of the frequency  $\omega$ . The inset shows the height of the steps which is described by a BESSEL function.  $\Phi_0$  is the magnetic flux quantum and defined as  $\Phi_0 = h/2e$ . The figure was taken from GROSS and MARX [18].

Often the impedance of the setup is not negligible, which makes it more realistic to consider current bias instead of voltage bias. The case of current bias is more

complicated as we end up with a non-linear differential equation that cannot be solved analytically. Calculations by RUSSER *et al.* [24] on an analog computer showed that the voltages for the SHAPIRO steps correspond to the voltages we know from the SHAPIRO spikes of ideal voltage bias. The step height, however, is only qualitatively, not quantitatively described by the BESSEL functions if the frequency is not much greater than  $2eI_cR_N/h$  [23, 25]. Assuming a resistance of  $R = 1/G_0$  and a critical current of the order of  $\sim \text{nA}$ , we obtain microwave frequencies in the GHz regime. The SHAPIRO steps for an overdamped and an underdamped JOSEPHSON junction in the case of current bias are presented in figure 2.7. The experimental data shown here comes from [26].

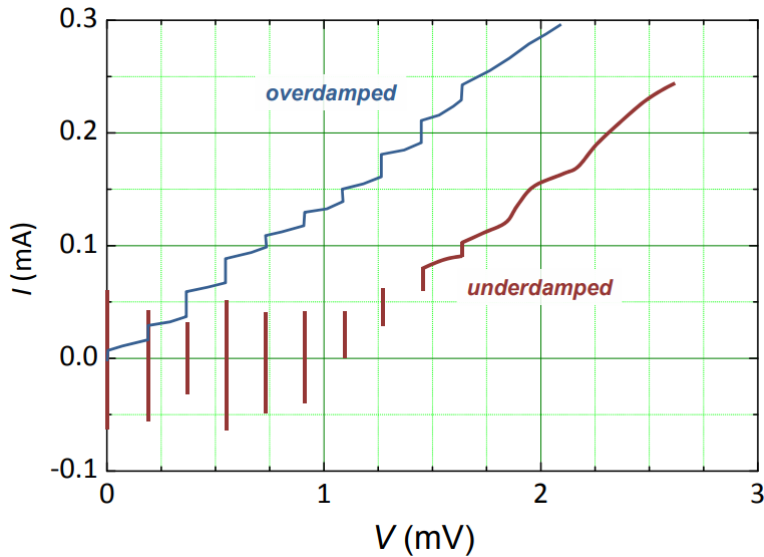


**Figure 2.7:** Overdamped and underdamped JOSEPHSON junctions show SHAPIRO steps under microwave irradiation in the case of current bias. The figure was taken from GROSS and MARX [18], the data comes from [26].

## 2.7 Photo-Assisted Tunneling

Inseparable from the discussion of the effect of microwaves on the supercurrent is the effect of microwaves on the quasi-particle tunneling current at the gap edges  $V_g = 2\Delta/e$ . SHAPIRO steps essentially replicate the supercurrent at zero bias, whereas photo-assisted tunneling (PAT) creates replicas of the gap edge. Both effects always happen simultaneously. TIEN and GORDON proposed a heuristic model [27] to explain the peaks around  $V_g$  in the  $dI/dV$ -curves for superconductor-insulator-superconductor junctions that are irradiated by microwaves [28]. The TIEN-GORDON equation describes the time-averaged dc tunnel current as

$$I(V_0, \omega, V_\omega) = \sum_{n=-\infty}^{\infty} J_n^2 \left( \frac{eV_\omega}{\hbar\omega} \right) \cdot I_0 \left( V_0 - \frac{n\hbar\omega}{e} \right) \quad (2.16)$$

where  $V_0$  is the dc bias voltage of the junction,  $\omega$  the frequency of the microwaves and  $V_\omega$  the corresponding local ac voltage amplitude caused by the microwaves.  $I_0$  is the quasi-particle tunnel current without microwave irradiation. There are three small but very important differences between the replicas caused by PAT on the quasi-particle tunnel current at the gap edges and the SHAPIRO steps that replicate the supercurrent. First, the voltage separation of the quasiparticle steps is twice as big as for the Shapiro steps because  $e$  and not  $2e$  appears in the denominator. Second, the steps are not truly flat meaning they have no constant voltage. The sharpness of the voltage replicates the sharpness of the increase of the quasiparticle current at the gap voltage. Third, the amplitude of the steps is described by the **square** of a BESSEL function with again a factor  $e$ , for quasi-particles, instead of  $2e$ , for Cooper pairs, in the argument. [7] A very clear example for PAT is presented in figure 2.8 as the applied microwave frequency is very high causing a large voltage separation of the steps and there are no higher-order contributions or supercurrent which would produce additional steps.

Note that the term "photo-assisted tunneling" is somewhat misleading, since electrons in the TIEN-GORDON picture do "absorb" or "emit" an integer number of electromagnetic quanta before tunneling elastically through the junction. However, there are no "real" photons involved. The behavior of the junction can be fully described by a classical electromagnetic field, the quantization of the electromagnetic field is not necessary here [29]. Estimations on the ponderomotive energy demonstrate that the junction is dominated by the classical electrical rather than the photon energy. This is shown in the supplemental material for reference [30].

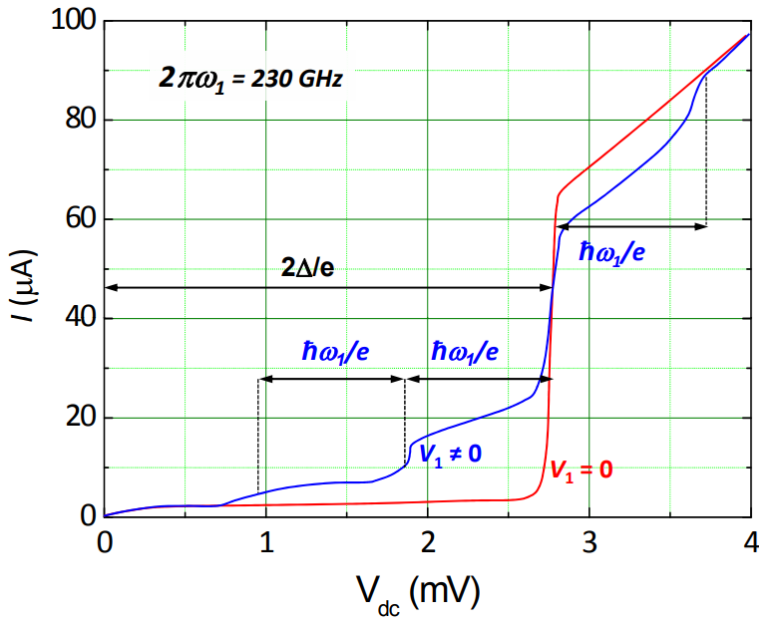


**Figure 2.8:** Photo-assisted tunneling on a superconductor-insulator-superconductor tunnel junction showing steps in the current-voltage curve at voltages  $V_n = V_g \pm n\hbar\omega/e$  that replicate the gap edge. The figure was taken from GROSS and MARX [18].

## 2.8 State of the Art of Research

In literature SHAPIRO steps and PAT are often discussed separately. There are various reasons for this. To begin with, the physical origin of the quasi-particle and the COOPER pair current is very different, which justifies to treat the two effects individually. However, in our experiments where we have atomic contacts with conductances of a few  $G_0$  the overlapping of the steps they create in the  $IV$ -curves is almost unavoidable. With frequencies in the 10 GHz range, we are not using particularly high frequencies. Previous experiments on Sn-SnO-Pb, for example, showed strong overlapping of SHAPIRO steps and PAT as well, but the frequency used here was considerably larger with 604 GHz [31]. One has to keep in mind that the energy gap  $\Delta$  for the aluminum we use is particularly small compared to other materials. As we know from equation 2.1, the gap energy  $\Delta$  is directly proportional to the critical temperature  $T_c$ . Taking a look at a table with the critical temperatures of commonly used superconductors, as shown in [23], for instance, one can see that most superconductors have a higher critical temperature  $T_c$  and thus a larger energy gap  $\Delta$  than aluminum. This might be a reason, why there is less overlap of the two effects in other systems. Furthermore, one can only observe SHAPIRO steps if the transmission of the junction is high enough and there is an appreciable supercurrent. For this reason many scanning tunneling microscope (STM) experiments only measure PAT but no SHAPIRO steps.

For junctions containing intermediate and high transmissions, not only SHAPIRO steps are enabled, but also higher-order processes like MAR and photon-assisted tunneling on the multiple Andreev reflections (PAMAR) under microwave irradiation. Strictly speaking, it would also be more correct here to speak of microwave-assisted MAR instead of photon-assisted MAR, but we will stick to this common term in the following.

When GREGERS-HANSEN *et al.* [32] first observed PAMAR in DAYEM bridges in 1973, they noticed, that the position of the peaks in the  $dI/dV$ -curves is

$$V_{m,n} = \frac{2\Delta}{me} \pm \frac{n\hbar\omega}{me} \quad (2.17)$$

with  $m$  being the order of MAR and  $n$  a natural number here. They further reported, that also the argument of the BESSEL function has to be adjusted via replacing the charge of a single particle  $e$  by  $me$  for the corresponding order of MAR. The PAMAR are therefore sensitive to the number electrons involved. This is also known from shot noise in point contacts [33, 34]. SOERENSEN *et al.* [35] further investigated PAMAR in niobium point contacts and presented the following equation

$$I(V_0, \omega, V_\omega) = \sum_{m=1}^{\infty} \sum_{n=-\infty}^{\infty} J_n^2 \left( \frac{meV_\omega}{\hbar\omega} \right) \cdot I_0 \left( V_0 - \frac{n\hbar\omega}{me} \right) \quad (2.18)$$

as a "natural generalization" of the TIEN-GORDON equation 2.16. This phenomenological equation is later confirmed by a theoretical model from first principles by

CUEVAS *et al.* [36] in 2002. Independently of this, ZIMMERMANN *et al.* [37] could find a theoretical derivation for the phenomenological position of the voltages as well.

A first direct and quantitative comparison between theory and experiment with good agreement has been demonstrated by CHAUVIN *et al.* [38], who also worked on a MCBJ made from aluminum as we do. However, our systems are not exactly similar, as they had an on-chip capacitor and resistor to get as close as possible to a perfect voltage bias and to dampen phase fluctuations as much as possible. Further details can be found in the doctoral thesis of CHAUVIN [39].

Also more recent publications discuss PAMAR. KOT *et al.* [30] extensively investigate the effects of microwaves in ultralow temperature STM experiments with vanadium tip and sample. PETERS *et al.* [40] probe superconducting tunnel junctions including an impurity-induced Yu–Shiba–Rusinov (YSR) state in an STM with lead tip and substrate and magnetic manganese adatoms. They find that the TIEN–GORDON model breaks down for tunneling via YSR states by resonant ANDREEV reflections. The work by SIEBRECHT *et al.* [41] shows that microwave irradiation can excite the YSR state by triggering a tunneling event and transferring a total of two charges. Another very current publication by HAXELL *et al.* [42] shows that caution is advised when it comes to attributing replicas to the presence of FLOQUET–ANDREEV states. Last but not least, the work of CARRAD *et al.* [43] demonstrates in PAMAR up to the order of  $m = 3$  in epitaxial InAsSb/Al nanowires.

Under certain conditions the replicas of the supercurrent at zero bias cannot be understood in terms of SHAPIRO steps, but rather as phase-incoherent tunneling of COOPER pairs that is described by a squared BESSEL function instead of the expression we know from equation 2.13. A theoretical description for this was given by FALCI *et al.* [44]

$$I_S(V_0, \omega, V_\omega) = \sum_{n=-\infty}^{\infty} J_n^2 \left( \frac{2eV_\omega}{\hbar\omega} \right) \cdot I_0 \left( V_0 - \frac{n\hbar\omega}{2e} \right) \quad (2.19)$$

which is very similar to the TIEN–GORDON equation. Experimental evidence for the incoherent tunneling of pairs comes from ROYCHOWDHURY *et al.* [45] who showed this effect in their STM measurements using a niobium tip and substrate. KOT *et al.* [30] do a great job explaining the origin of phase-incoherent tunneling of COOPER pairs in the supplemental material of their paper. The reason for the breakdown of the expression for the supercurrent as given in equation 2.13 is that the phase difference between the two superconductors is not well defined anymore (“the phase difference  $\varphi$  is no longer a good quantum number”) as the low capacitance of the junction leads to a significant charging energy  $E_C = e^2/2C$ . Combined with cryogenic temperatures, this leads to the dynamical Coulomb blockade (DCB) effect, which comes with large quantum fluctuations and incoherent tunneling of COOPER pairs. The environment basically acts as a second junction which then leads to the Coulomb blockade effect [46]. The incoherent tunneling of COOPER pairs was also discussed recently in the previously mentioned publications by PETERS *et al.* [40] and CARRAD *et al.* [43] who confirm the results of ROYCHOWDHURY *et al.* [45].

Very high transmissions lead to non-sinusoidal current-phase relations which give rise to non-integer SHAPIRO steps, which are often also called fractional or subharmonic SHAPIRO steps. The deviation from a sinusoidal current-phase relation as stated in the first Josephson equation 2.7 is also often referred to as skewed current-phase relationship. These fractional SHAPIRO steps have already been observed by DAYEM *et al.* [47] in 1967, for example, showing fractional steps down to 1/8. Also from the theoretical side, the fractional SHAPIRO steps are well understood as the microscopic theory by CUEVAS *et al.* [36] shows. The subharmonic steps are directly related to the MARs which were also discussed in this publication.

Current publications on fractional SHAPIRO steps, among other aspects deal with large arrays of JOSEPHSON junctions [48, 49] that have a skewed current-phase relation or JOSEPHSON junctions based on highly transmissive nanowires [50, 51] or nanoflags [52] that show half-integer SHAPIRO steps.



## 3 Setup and Samples

In this chapter I want to briefly describe our setup and the samples we have been measuring. This includes the cryogenic system, the mechanics for the MCBJ as well as the electronic devices that have been used and their arrangement. An important part of my work was to install new microwave cables and characterizing them. The types of measurements and the samples used as well as their fabrication is discussed here as well.

### 3.1 Cryogenics and Mechanics

The superconducting SET experiment comes with certain requirements to the setup. First, the temperature should be well below  $T_C$  in order minimize thermal rounding IVs. As we use aluminum, we need  $T \ll 1.2\text{ K}$ . Furthermore, we want to avoid thermal fluctuations on the SET. Therefore, we have to ensure  $E_C > E_{\text{th}} = k_B T$  with the charging energy  $E_C = e^2/2C$  of the superconducting island where  $C$  is the island's capacity. This is another reason for performing the experiment at milli-Kelvin temperatures.

As we want to irradiate our samples with microwaves, the cryostat must not only reach a sufficiently low base temperature, but also provide enough cooling power to compensate for the heating effect of the microwave irradiation. The BlueFors LD400 is a commercial dry dilution fridge and comes with a base temperature of  $10\text{ mK}$ . With all the cables that have been installed we can still reach temperatures close to  $30\text{ mK}$ . BlueFors specifies a cooling power of  $14\text{ }\mu\text{W}$  at a temperature of  $20\text{ mK}$  and a cooling power of  $400\text{ }\mu\text{W}$  at a temperature of  $100\text{ mK}$ . In a rough estimate, neglecting JOULE heating from the electronic measurements, microwave powers of up to  $-20\text{ dBm} (= 10\text{ }\mu\text{W})$  should be possible at temperatures close to base temperature and powers up to  $-4\text{ dBm} (= 398\text{ }\mu\text{W})$  should result in temperatures around  $100\text{ mK}$ . Details on the BlueFors can be found in the dissertation of Martin Prestel [53] who took the cryostat into operation.

I would just like to name the most important features of the cryostat, which are relevant for our experiments. The BlueFors is equipped with a superconducting magnet with magnetic field in the z-direction, which corresponds to an out-of-plane magnetic field as the z-direction is perpendicular to the surface of the sample. There is currently no possibility to control the sample temperature, but a sample heater with the associated temperature control are in planning. In order to utilize the full output range of our voltage source, we replaced the 1:10 voltage divider which is coupled to the 4 K-plate inside the cryostat by a 1:100 voltage divider which is presently located at room temperature allowing for more flexibility.

The mechanics for the break junction comes with a very high gear ratio resulting in precise control to open and close the atomic contacts and very stable contacts enabling long measurements. A schematics of the three-point bending mechanism is shown in figure 1.1. There are two counter supports and a pushing rod moving along the z-axis, which is bending the sample downwards against the counter supports. Other than shown in the figure, the sample is mounted upside down in the cryostat.

The mechanics was taken apart after a blockage, cleaned and reassembled in September 2023. There are two types of bearings: friction type bearing and ball bearing. Only the latter is suitable for cold temperatures. All spare bearings have now been labeled. All pumps (except for one scroll which is only necessary for condensing) have been maintained according to instructions from BlueFors in November 2022.

## 3.2 Electronics

Low temperature experiments with small electric circuits require a variety of electronic devices. Since our measurements are very sensitive to noise, careful grounding is important. Figure 3.1 shows the most relevant devices for our measurements and their grounding scheme. The measurement ground is basically floating as everything is only connected to the cryostat which serves as a stable reference potential.

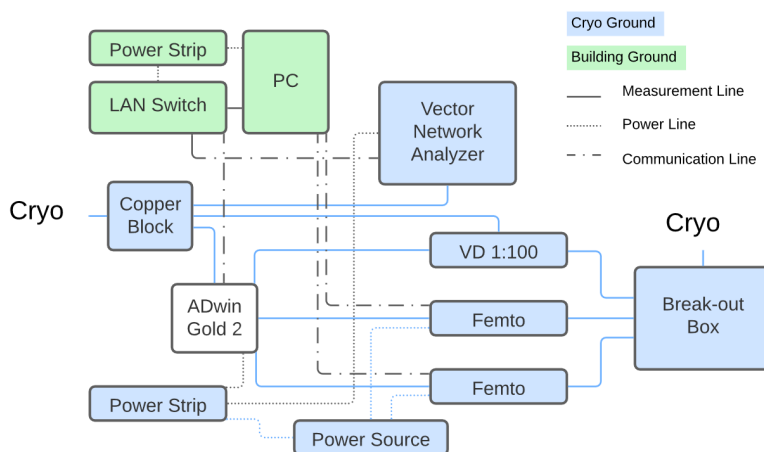


**Figure 3.1:** Grounding scheme showing the most important electronic devices and the way they are connected to each other.

We are using an ADwin-Gold II both as our voltage source and for controlling our measurements. The ADwin was carefully tested against other voltage sources and proved to be the superior choice. Different amplifier models were compared as well. Here, the Femto amplifier showed the lowest noise level of all available amplifier models.

In all experiments on atomic contacts under microwave irradiation of different frequencies and power or in magnetic field, we measure current and voltage at the MCBJ. The measurement scheme for this type of measurement is shown in figure 3.2a. The voltage can directly be measured across the junction, while the current is determined via a voltage measurement of a reference resistor of  $\sim 50\text{ k}\Omega$ . This reference resistor is thermally coupled to the still plate in the cryostat which is at a temperature of  $\sim 1\text{ K}$  and was measured to be  $51.689\text{ k}\Omega$ .

For measurements of the virgin state sample, however, we had to adapt the measurement geometry, as these samples have significantly lower resistances than the

reference resistors, which causes a great measurement uncertainty on the current measurement. To avoid this problem, we source the sample via the cables we have been previously using to measure the voltage, while measuring the voltage with the original bias cables. The current can now be determined through a voltage measurement on a small reference of  $100\Omega$  at room temperature as shown in figure 3.2b.

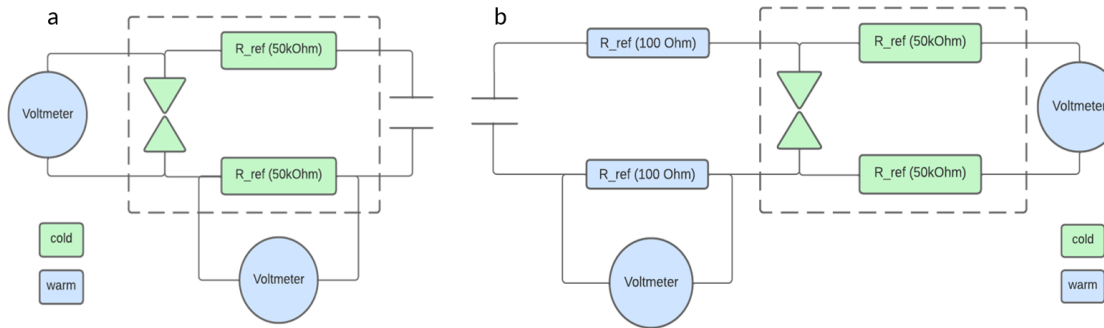


**Figure 3.2:** Measurement scheme showing the geometry of the current and voltage measurement for (a) high-Ohmic and (b) low-Ohmic samples. The current is determined through a voltage measurement of a reference resistor of comparable resistance.

### 3.3 Microwave Irradiation

We use a vector network analyzer (VNA) and microwave source and coaxial cables to transmit the microwave irradiation to our sample. The cables used to connect the VNA to the cryostat are commercial ones from Huber+Suhner and the cables inside the cryostat all the way down to the mixing chamber plate (innermost/coldest temperature stage) were preinstalled by BlueFors. The microwave cables and the connectors between the sample and the mixing chamber plate were made by ourselves.

When it comes to precise microwave irradiation flip-chip method using a waveguide is ideal. This method requires a stationary sample, which unfortunately is not the case with our three-point bending mechanism of the MCBJ. A possible solution to this problem would be a two-point bending mechanism as presented by JANVIER *et al.* [54] or in even more detail in the doctoral thesis of BRETHEAU [55] who worked on the same setup. As this would require major changes to the setup we opted for a simpler solution. An antenna which is created by stripping a coaxial cable is probably the simplest method to emit microwaves. Figure 3.3a shows our antenna inserted through the sample holder from above. The shiny silver part in the center of the image is the inner conductor, which has been exposed by stripping the coaxial cable.

As we were afraid, that the movement of the sample when opening and closing the MCBJ would change the distance to the microwave antenna and therefore the local power significantly, we decided to install a second microwave cable which is connected to an on-chip stripline and test the two microwave transmitters against each other.

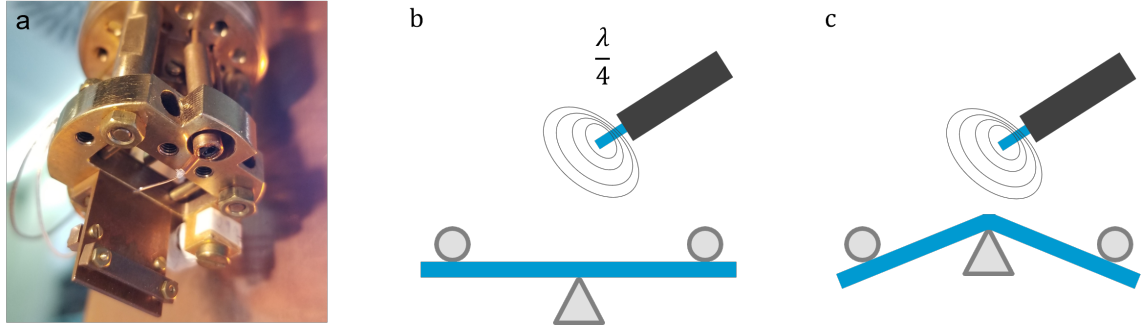


**Figure 3.3:** (a) Image of the antenna used for microwave irradiation. Concerns on how bending the sample might change the local power through changing the distance between sample and antenna are visualized in (b) and (c).

A sketch of the closed MCBJ (flat substrate) and the open MCBJ (bent substrate) is shown in figure 3.3b and 3.3c. An overview of the sample design with the on-chip stripline is presented in figure 3.4a next to a zoom on the MCBJ-SET in figure 3.4b. The stripline is positioned very close to the MCBJ-SET to transmit the maximum power possible. The distance between MCBJ-SET and stripline stays constant regardless of the degree of bending of the substrate.

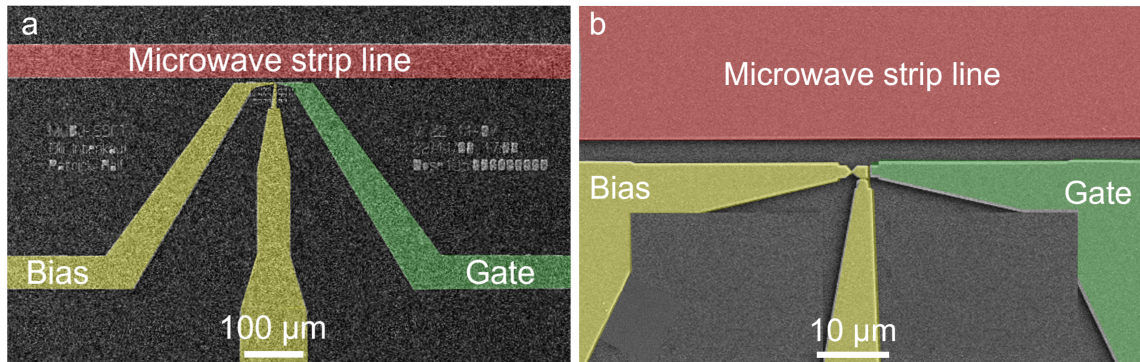


**Figure 3.4:** False color scanning electron microscope image of the sample showing (a) an over view of the sample design and (b) a zoom on the MCBJ-SET.

Other than expected, initial concerns on the variation the local power due to the bending of the sample are rather unjustified as the following estimations show after having installed the antenna. The total range of motion of the sample is  $\sim 5$  mm which corresponds to 13 full rotations of the differential screw which is moving the pushing rod and thus bending the sample. As within less than one rotation of the differential screw we can change a contact from fully closed ( $G > 40G_0$ ) to fully open ( $G < 0.05G_0$ ), an upper limit for the actual movement of the sample would be  $5\text{ mm}/13\text{ rotations} = 0.4\text{ mm}$ . Comparing that to the distance ( $d \geq 10\text{ mm}$ ) between sample and antenna, this results in a variation of the distance  $d$  of  $\sim 4\%$  or  $\sim 8\% < 1\text{ dB}$  of power assuming that the microwave power scales as  $P_{\text{MW}} = 1/d^2$ .

### 3.4 Sample Fabrication

Before subjecting a MCBJ-SET to microwave irradiation, we wanted to test our newly installed microwave cables with a simpler experiment, especially for comparing them against each other. This is why we took a step back from the MCBJ-SET and fabricated just a superconducting MCBJ made from aluminum, but in the same geometry the sample design of the SET has. I described the fabrication of a superconducting SET in great detail in my "Projektpraktikum" (PP) report [56] and therefore refrain from further details here. A summary of the steps required for fabrication can be found in table ?? in the appendix.

The sample design was adopted from the predecessors in this project [4, 6], where essentially only the layout of the leads was changed in order to create space for the additional microwave stripline and allow for easier contacting. To avoid alignment problems which would be necessary when doing multiple steps of electron-beam lithography, we included the stripline in the design for our single-step lithography.

We simplified the sample design of the MCBJ-SET in two ways, both implementing only a simple aluminum MCBJ. The first simplification only omits the oxide barrier that would be necessary for the SET, while keeping the original fabrication procedure including shadow evaporation exactly as described in my PP report [56]. Being composed from two layers of aluminum (50 nm + 70 nm) the sample shown in 3.5a has second constriction in form of a finger contacting the island from below which is comparable in size to the MCBJ. To remove this second constriction we developed the second simplification which is presented in figure 3.5b. Here, we enlarged the lead which was contacting the island contacting effectively removing the island and the second constriction. For this type of sample we only evaporated 80 nm without the need for shadow evaporation.

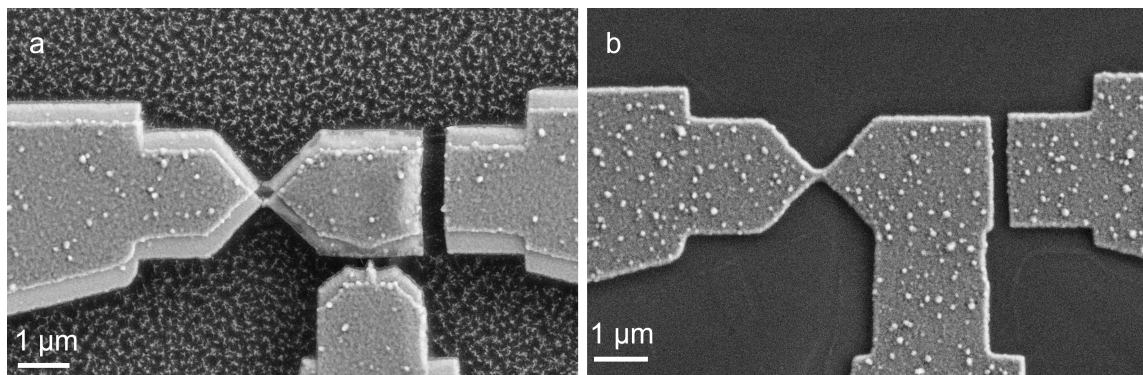


**Figure 3.5:** Simplified sample designs in the MCBJ-SET geometry with (a) the original lithography mask and (b) an enlarged lead to remove the second constriction. The background in (b) looks different as the sample in (a) has already been etched before taking the SEM image.



## 4 Measurements and Results

We have measured a total of four samples, of which two each are twin-samples meaning that they have the same geometry and that they were evaporated at the same time. The first two samples correspond to the first simplification of our sample design. Here, we used the MCBJ-SET sample geometry that already existed [4, 56] and just omitted the oxidation step between the two layers of aluminum, that are deposited by shadow evaporation. The contacting of the island therefore is accomplished by a 100 nm wide finger, but without the oxide barrier that would be present in an SET. Samples from this type are referred to as "S1a" and "S1b". The other two samples, denoted as "S2a" and "S2b", are of the type of the second simplification where the 100 nm finger was replaced by a lead with the width of the island.

A brief overview of the four samples and the types of measurements carried out with them is presented in table 4.1. These measurements are namely the characterization of low-Ohmic contacts (virgin sample before opening the MCBJ for the first time) in magnetic field, the magnetic field study for atomic contacts (open MCBJ) and the study of the frequency and power dependency on the microwave excitation. As can be seen at first glance, the majority of data comes from sample S2b. What happened to the other samples and why we switched samples will be discussed in detail later.

**Table 4.1:** Overview of the four samples measured and the type of measurements performed. The two samples S1a and S1b as well as S2a and S2b are duplicates of each other.

	Low-Ohmic Contacts	Atomic Contacts	Microwave Effects
<b>S1a</b>	✓	-	-
<b>S1b</b>	✓	✓	-
<b>S2a</b>	✓	-	(✓)
<b>S2b</b>	✓	✓	✓

### 4.1 Low-Ohmic Contacts

To start the characterization of our samples we were first interested in their superconducting properties before opening the MCBJ as it is impossible to return to this virgin state. We therefore measure voltage and current at the sample for different magnetic fields starting with a magnetic field in negative z-direction, which is stronger than the critical magnetic field. Then we increase the magnetic field in steps of 0.25 mT until we surpass the critical magnetic field in positive z-direction.

Once the critical magnetic field has been exceeded, our aluminum sample switches from its superconducting state to the normal conducting state following an Ohmic current-voltage relation. The same happens when exceeding the critical current. As soon as the sample is normal conducting, JOULE heating quickly increases the

temperature to above 400 mK which is one order of magnitude higher than our base temperature. This heating for measuring low-Ohmic contacts with currents in the milli-Ampere range is inevitable as the setup has been optimized for high-Ohmic samples and therefore low currents. To be able to measure the low-Ohmic contacts in the first place, we had to adapt the measurement circuit shown in figure 3.2b. The main difference is that the current measurement is now realized with a  $100\Omega$  reference resistor at room temperature instead of the  $\sim 50\text{ k}\Omega$  reference resistor which is thermally coupled to the still plate ( $\sim 1\text{ K}$ ).

The  $IV$ -measurement of a low-Ohmic contact (S2a in this example) is presented in figure 4.1. We have current bias, because the cable resistances cannot be neglected compared to the sample resistance. The blue curve shows the  $IV$ -characteristics for a down-sweep, the orange curve is its numerical derivative  $dI/dV$ . There are two critical currents  $I_{C,1}$  and  $I_{C,2}$  as well as two retrapping currents  $I_{R,1}$  and  $I_{R,2}$  which differ from the critical currents. The jumps in the  $IV$ -curve for critical current and retrapping current translate to spikes in the  $dI/dV$  which basically shows the slope of the  $IV$ -curve and therefore the resistance of the sample. For large bias currents  $I_{\text{Bias}} > I_{C,2}$  the slope approaches the normal resistance  $R_N$ .

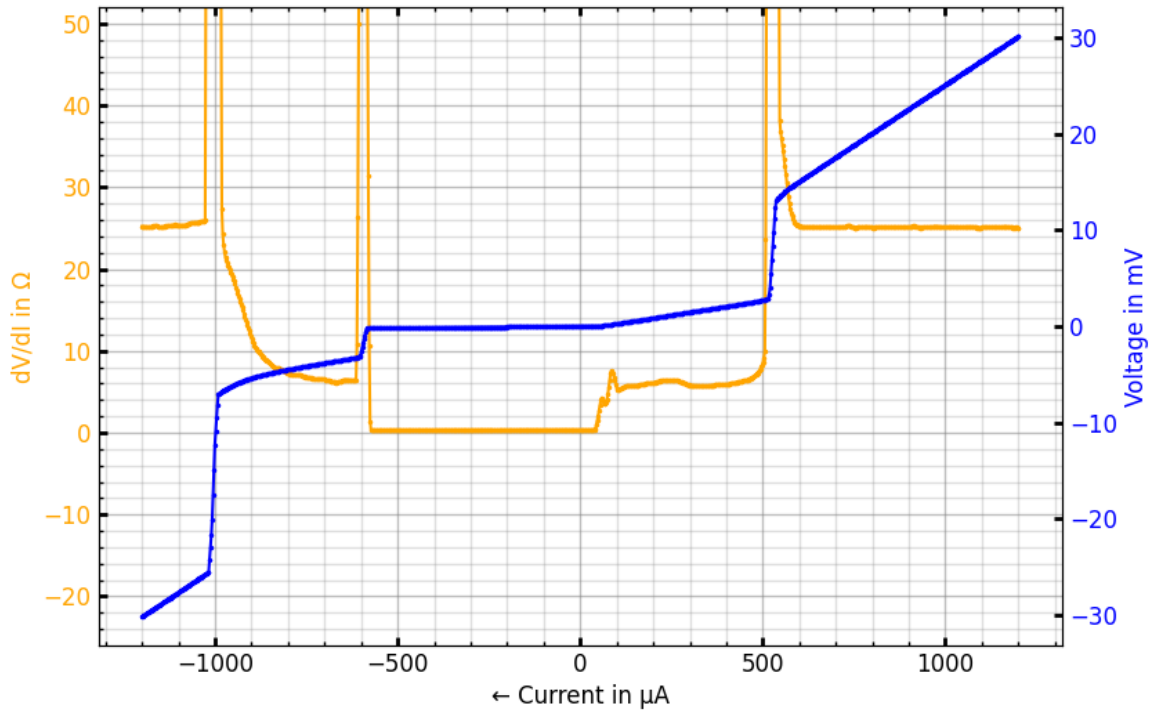


**Figure 4.1:** The blue curve shows the  $IV$ -characteristics for a down-sweep on sample S2a at zero magnetic field. In this example, the bias current is large enough to overcome both critical currents ( $I_{C,1} \approx -600\text{ }\mu\text{A}$  and  $I_{C,2} \approx -1000\text{ }\mu\text{A}$ ) of the sample. The  $dI/dV$  is shown in orange and reveals a double peak structure for the retrapping current close zero bias.

If we now measure  $IV$ -curves for different magnetic fields and calculate the  $dI/dV$ , we can obtain a color map as shown in figure 4.2. Here, the bias current is given on the

x-axis (up-sweep in 4.2a and down-sweep in 4.2b), the applied magnetic field on the y-axis and the color bar shows the  $dI/dV$  and therefore the sample's resistance. The data points on the left show the temperature at the sample thermometer measured during the  $IV$  sweeps for different magnetic fields.

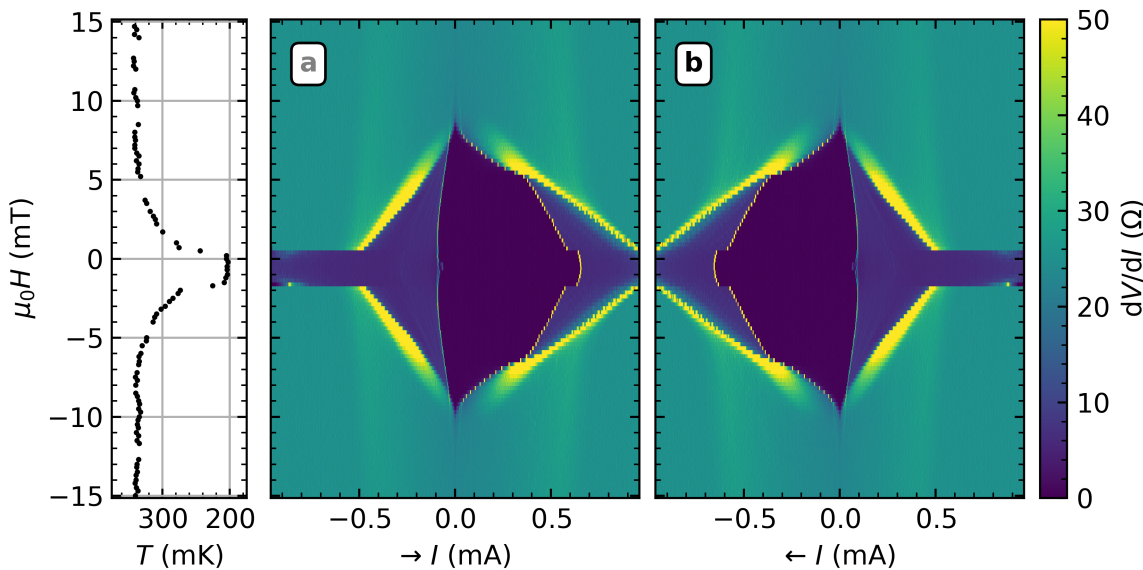


**Figure 4.2:** Magnetic field study on a low-Ohmic contact showing (a) an up-sweep and (b) a down-sweep. The measurement is hysterical and symmetrical with respect to the sweep direction, as the comparison between up-sweep and down-sweep shows. In this example, for small magnetic fields, the bias current is not large enough to exceed both critical currents of the sample. As a consequence, the temperature in stays significantly lower for these magnetic fields.

There are three main areas of sample resistance: a dark purple area in the center, which is surrounded by a blue area from left and right and a greenish background. The dark purple colored area has a resistance very close to  $0\Omega$ , this is where all parts of the sample are superconducting. The boundary lines of this area are the critical current  $I_{C,1}$  and the corresponding retrapping current  $I_{R,1}$ . A peculiarity of this measurement is, that the bias current was chosen too small to exceed the critical current  $I_{C,2}$  of the leads for small magnetic fields. Only for an increased magnetic field, we can observe the critical current  $I_{C,2}$  and retrapping current  $I_{R,2}$  as well. There is a small offset of approximately 0.75 mT on the magnetic field axis, which is very visible in the temperature plot on the left. This data also clearly shows how the temperature increases due to Joule heating as an increasingly larger part of the  $I - V$  sweep is becoming normal conducting for increasing magnetic fields. At a magnetic field strength of  $\sim 10$  mT the sample finally changes its state to normal conducting and the temperature during the  $I - V$  sweep stays constant. The normal conducting resistance  $R_N$  is approximately  $25\Omega$  and results in a uniformly colored background for parts of the  $I - V$  sweep that exceed the samples critical current and critical magnetic field. The only exception to this monochrome background is a very pale

feature around  $\pm 0.5$  mA, which seems to vanish only at very high magnetic fields. Since only sample S2a shows this feature and we could not find a reason for this, I will not go into it further.

When comparing up-sweep and down-sweep one can notice, that the color map is symmetrical with respect to the current sweep direction but apart from that, there is not much of a difference. For this reason, I will only discuss the up-sweep in the following.

Figure 4.3 compares the two samples from the type of the first sample simplification. Figure 4.3a shows the first magnetic field study we performed on a closed MCBJ. The data for this comes from sample S1a and is the only data set we have from this sample as it died soon after the measurement. The figures 4.3b and 4.3c both show measurements from sample S1b but for different amplitudes of the bias current. Comparing the measurements for S1a and S1b, we can notice, that the measurement of S1a is overall noisier and the background color is greener than for S1b. The noise problem disappeared when changing to sample S1b. However, similar problems arise again and can be solved by changing one of the amplifiers. The difference in the background color can be explained by a slight discrepancy of the normal resistance of the two samples. Even though the figures 4.3a and 4.3b have been measured with the same amplitude of bias current and comparable mean temperature, the maps show some differences. In 4.3a the bias current was not sufficient to exceed the critical current  $I_{C,2}$  for magnetic fields smaller than  $\sim 8$  mT, in 4.3b the bias current was not even sufficient to overcome  $I_{C,1}$  for small magnetic fields. This indicates stronger superconductivity for sample S1b as it almost takes twice the bias current to leave the area where the sample is all-superconducting while causing significantly more heating.

An SEM image taken after the measurement revealed, that sample S1a broke the 100 nm thin finger which is contacting the island. We can assume that the connection via the finger in sample S1a was weak in the first place, as S1a shows reduced critical current and a thin feature for  $I_{R,1}$  and  $I_{C,1}$  at enhanced critical magnetic fields compared to S1b. A narrower constriction as the weakened finger of S1a represents one is known to have smaller critical currents and higher critical magnetic fields. A more fragile finger for sample S1a therefore fits in this picture and is a possible explanation for the death of this sample.

The circumstance of the disconnected finger and the rather complicated features at the retrapping current  $I_{R,1}$  has motivated us to simplify the sample design further. The 100 nm thin finger was replaced by a lead with the width of the island making the closed MCBJ the only constriction in this sample geometry. A comparison of the two sample types is presented in figure 4.4, the insets show SEM images of the samples as a reminder of their geometry. The temperature during these two measurements and the amplitude of the bias current are comparable, yet not identical, as the critical current  $I_{C,1}$  would not have been exceeded for the same amplitude of bias current. Comparing the two types of sample simplifications side by side one can clearly see that the critical currents  $I_{C,1}$  and  $I_{C,2}$  in 4.4a are weaker than in 4.4b, whereas the critical magnetic field is enhanced. Having the critical magnetic field of bulk aluminum in mind, which is  $\sim 10$  mT, and knowing that reduced dimensions show enhanced critical

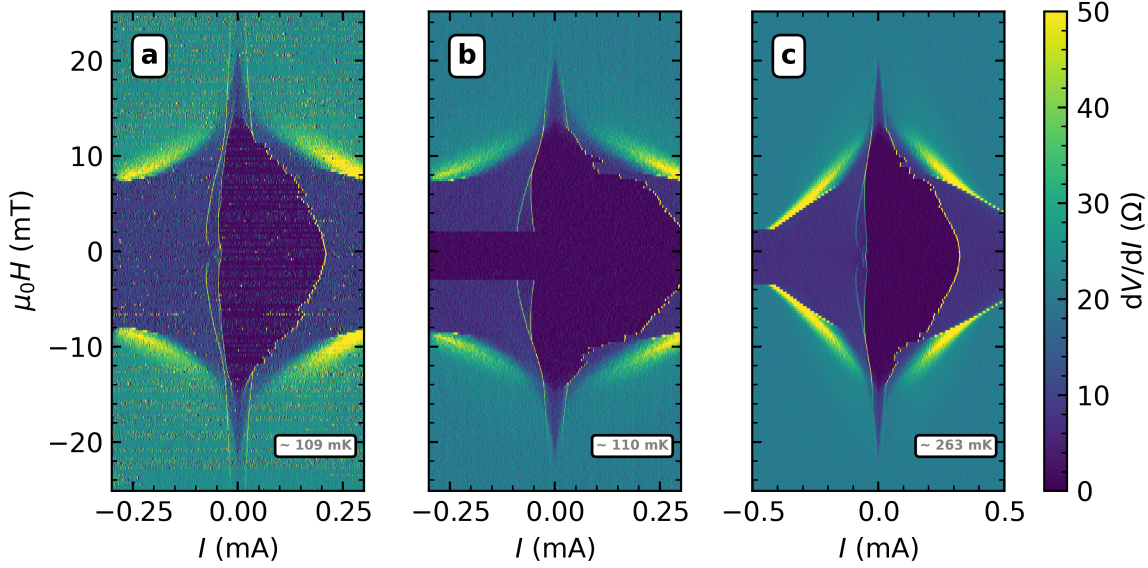


**Figure 4.3:** A comparison of the two samples from the type of the first sample simplification for a magnetic field study under similar conditions is shown in (a) and (b). Since sample S1b showed stronger superconductivity, the bias current was increased in (c) to be able to overcome  $I_{C,1}$ .

magnetic fields, one can argue that the first sample simplification is in the thin film limit while the second sample simplification is better described by the bulk limit. The enhanced critical current visible in 4.4b also fits into this argumentation. For the first sample simplification we evaporated 70 nm of aluminum on top of 50 nm via shadow evaporation. As there is no tunnel barrier in between the two layers that results in a total thickness of 120 nm. The second sample simplification on the other hand required no shadow evaporation and is therefore only one layer of aluminum with a thickness of 80 nm. Nevertheless, the film thickness at the constriction (MCBJ and finger) is thinner for the first sample simplification in 4.4a which limits the overall critical current and enhances the critical magnetic field to values higher than those expected from bulk aluminum.

The more complicated features at the retrapping current  $I_{R,1}$  shown in 4.4a can be attributed to the fact that there is a second constriction of comparable size in addition the MCBJ. Probably, the finger is even the stronger constriction due to the overlapping of the two aluminum layers caused by the shadow evaporation and the fact that the shadow of the MCBJ might be connected as well before opening the break junction for the first time, which we have not done yet. This means for the two samples S1a and S1b we have two constrictions in parallel. To avoid having the shadow bridge in the future, one has to take a closer look at the shadow evaporation. Possibly the undercut of the bilayer resist is too large allowing for the shadow bridge to be deposited on the substrate instead of the wall of the mask. Interestingly, the critical current  $I_{C,1}$  in samples from the type of the first sample simplification show no jumpy behavior at magnetic fields close to the critical field for maximum current amplitude, whereas for the second type it does. The temperature logs of 4.4b show

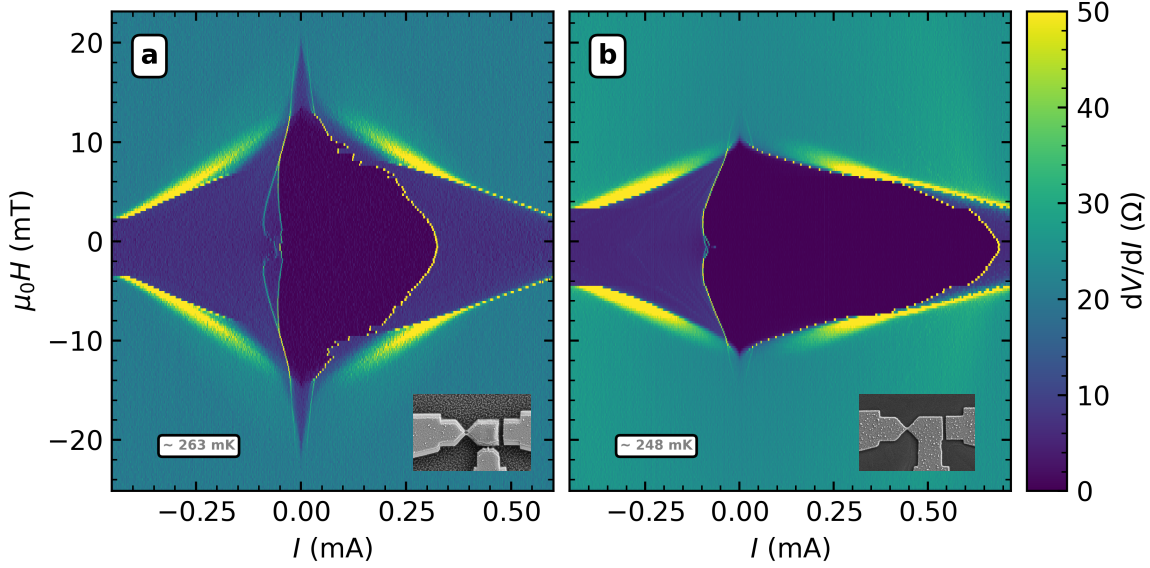


**Figure 4.4:** Magnetic field studies comparing the samples (a) S1b and (b) S2a which are type of first and second sample simplification. The insets show SEM images of the corresponding sample design and were taken from figure 3.5. (a) shows higher critical magnetic fields, whereas (b) shows higher critical currents.

a sudden drop in temperature at the same magnetic fields where we can observe the jump in  $I_{C,1}$  very similar to the temperature data presented in 4.2. Unfortunately, the temperature recordings for the first measurements (S1a and S1b) are incomplete, but there is no sign of a sudden temperature drop.

Even more alike than the samples S1a and S1b are the samples S2a and S2b, which are presented in 4.5. They have normal resistances of  $25.2\Omega$  and  $23.5\Omega$ , and very comparable critical currents. The critical magnetic field however is slightly reduced, which can be explained by aging of the sample as both samples were fabricated at the same time, but sample S2b was stored at ambient conditions for a few weeks before measurement. Due to issues with blocked mechanics we lost sample S2a before we could measure atomic contacts with this sample. As the figures 4.5a and 4.5b show, the two samples are very comparable and what we previously discussed for S1b and S2a therefore also applies for sample S2b.

## 4.2 Atomic Contacts under Microwave Irradiation

In this chapter we will discuss the effects of microwave irradiation on atomic contacts of different transmissions. We will start by analyzing a tunnel contact with very low  $G$  as the only effect we can observe here is PAT at the gap edges. As we continue with contacts of higher  $G \approx 2G_0$ , additional channels with different transmissions start to contribute to the electronic transport. Every contact is analyzed for its individual set of transmissions (PIN code), which can be obtained by fitting an  $IV$ -curve in the absence of microwave irradiation. As soon as there is a non-negligible supercurrent,

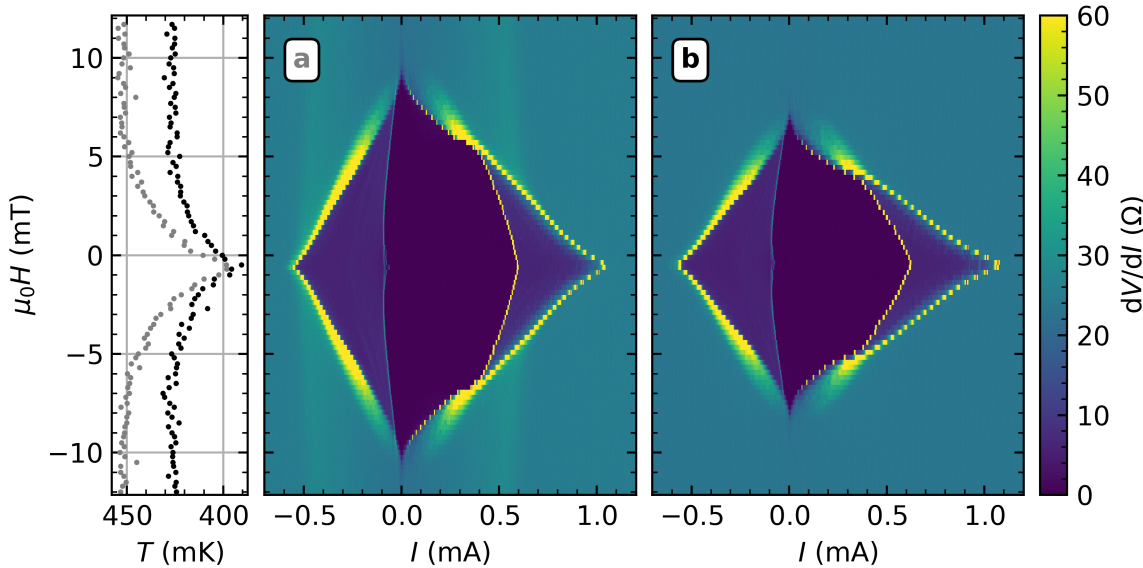


**Figure 4.5:** Comparison of two samples from the type of the second sample simplification. (a) could only be measured as a low-Ohmic contact with a closed MCBJ. All measurements with atomic contacts under microwave irradiation were performed on the sample shown in (b).

we start to see Shapiro steps fanning out from zero bias in addition to the PAT at the gap edges. For increasing transmissions we also start to see higher order tunnel processes and corresponding PAMAR under microwave irradiation. For very high transmissions, fractional Shapiro steps show up. All measurements can be reproduced to some extent by simulations according to the theory presented in chapter 2. The deviations can be understood by comparing our experiments to recent work of others and will be discussed in the following paragraphs.

The VNA can output microwaves up to 40 GHz and powers between  $-30$  dBm and  $0$  dBm. We can thus perform frequency studies, which means measuring  $IV$ -curves for different frequencies at a fixed power or power studies, where the output power is varied for a fixed frequency. Increasing the power naturally increases the temperature, but the microwave frequency also has an effect on the temperature as different frequencies have different transmissions through the microwave cables and they are subject to complex cavity effects. As the sample holder and the copper shielding (cylinder with  $r \approx 3$  cm,  $h \approx 10$  cm) are of the same length scale as the used microwave wavelengths. This can cause constructive and destructive interference, which is difficult to understand in detail. Figure 4.6 shows the temperature for a frequency sweep together with the reflected power measured by the VNA. Without going too much into detail here, one can clearly see an anti-correlation of the temperature and the reflected power, e.g., a correlation with the transmitted power, as expected.

All microwave connectors used in the setup are of the type SMA that are specified up to 26.5 GHz. However, the effective maximum frequency at moderate power that shows microwave effects in our measurements is approximately 20 GHz. This is shown in the frequency study of a  $\sim 4 G_0$  contact at  $-20$  dBm in figure 4.7a. The color map

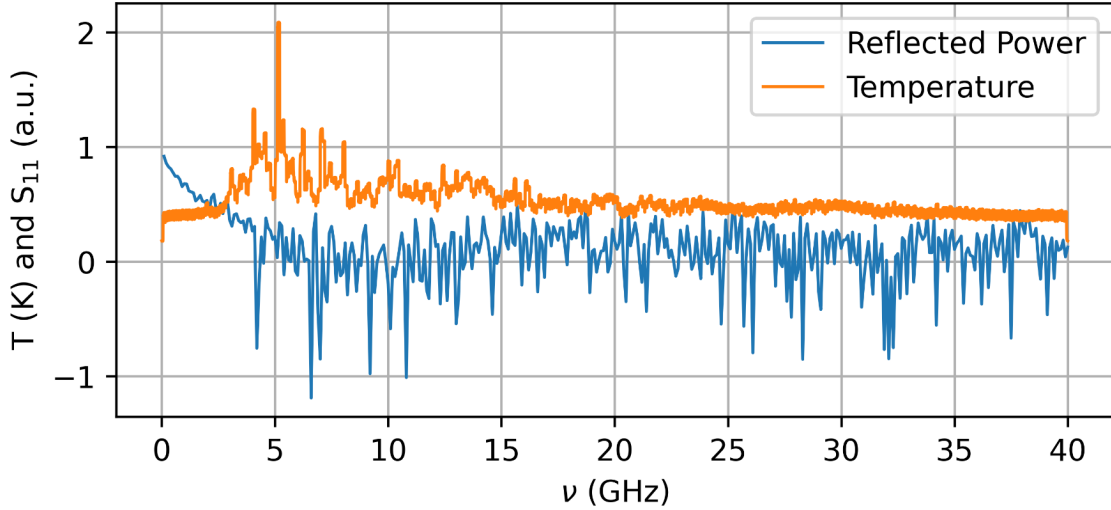


**Figure 4.6:** The temperature the reflected power  $S_{11}$  measured by the VNA during a frequency sweep are anti-correlated as shown in this measurement for the antenna. The course of the temperature curve for the stripline looks slightly different than for the antenna, but is also related to the reflected power.

shows a strong supercurrent and MAR up to the order of  $m = 4$  with a rich pattern of SHAPIRO steps and PAT that suddenly stops at  $\sim 20$  GHz. For this reason, we only measured up to frequencies of 20 GHz in most frequency studies. Interestingly, there are microwave effects showing up at frequencies between 30 GHz and 40 GHz for very high microwave powers. Figure 4.7b shows a contact with a total conductance of  $\sim 1 G_0$  contact at a microwave power of 0 dBm. Here, the lower part of the color map is heavily smeared due to the strong increase of temperature caused by the heating effects of the microwaves. The temperature rises to  $\sim T_c/2$  and partially even exceeds the critical temperature. This is why we stick to smaller output powers.

As the VNA outputs microwaves with a power in units of decibel-milliwatts (dBm), we used this logarithmic unit for our measurements. A color map of power study therefore looks as presented in figure 4.8a. For the analysis and comparison with the theory, it makes sense not to put the power in dBm but a local amplitude in the form of voltage on the y-axis. This is why we had to linearize the y-axis which leads to a logarithmically spaced point density for the output voltages. As a consequence, the pixel height increases with the power clearly limiting the power resolution. The result of the power axis linearization is shown in figure 4.8b, additionally the voltage axis has been normalized to the gap energy  $\Delta$ . In retrospect, it would have made sense to measure higher powers with increased point density and the output voltage in mind. I recommend adjusting the point density on the power axis for future power studies.

#### 4.2.1 Tunnel Contact

When opening the MCBJ very far, we can create a tunnel contact with a high resistance. The tunnel contact presented here shows a resistance of  $\sim 250$  k $\Omega$ , e.g., a

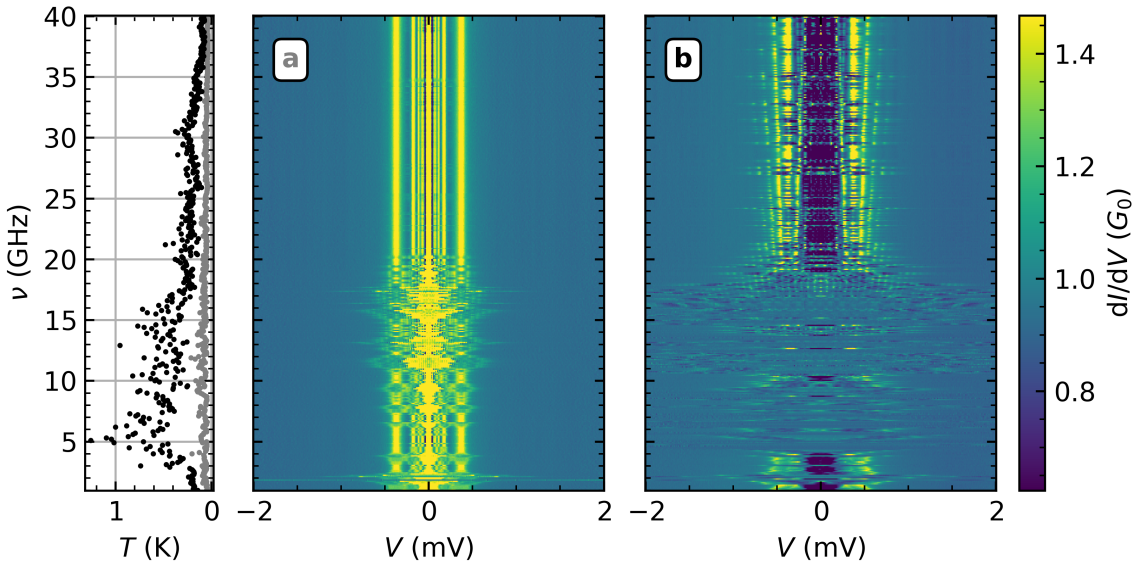


**Figure 4.7:** Comparison of two frequency studies at (a) low and (b) high microwave power. (a) shows a contact with  $\sim 4 G_0$  and microwave power of  $-20$  dBm, (b) shows a contact with  $\sim 1 G_0$  and microwave power of  $0$  dBm. To get achieve contrast for both color maps, the conductance of (a) was divided by four. For low powers, frequencies above  $\sim 20$  GHz show no microwave effects. High powers enable microwave effects for frequencies greater than  $\sim 20$  GHz, but cause an increase in temperature, especially at low frequencies.

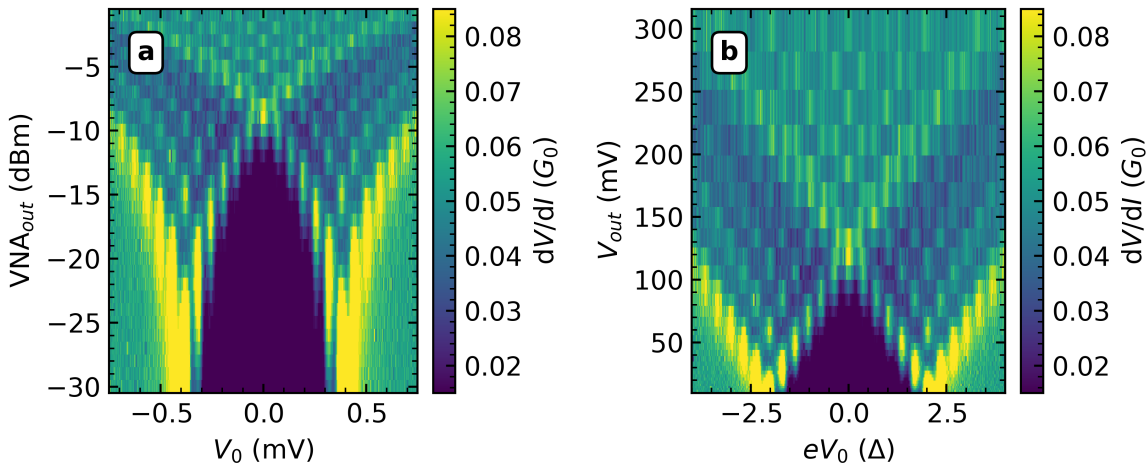


**Figure 4.8:** Power study showing the data (a) before and (b) after linearization. Additionally, the x-axis has been normalized to units of the gap energy  $\Delta$ . Before the linearization, the power axis was scaled logarithmically, now the pixel height scales logarithmically with the output voltage of the VNA.

conductance of  $\sim 0.05 G_0$ . A low total conductance implies that also the leading transmission is small. In fact, the analysis of the PIN code revealed, that only one transport channel with a transmission of  $\tau = 0.05$  contributes to the electronic transport. The fitting algorithm to determine the transmissions of the individual channels that contribute to the electronic transport is based on theoretical calculations by CUEVAS *et al.* [14]. Figure 4.9 shows (a) the measured *IV*-curve in blue and the fit as a dashed line in orange, and (b) the  $dI/dV$  calculated from (a). The measurement data has been smoothed with a SAVITZKY–GOLAY using a first order polynomial and a window length of  $1/1000$  of the array length. Likewise the same holds true for the color map data of the frequency and power study. The fit accurately reproduces the quasi-particle current at the gap edges and also finds remainders of ANDREEV reflections, which are only weakly pronounced in the measurement data. The reason why the features in the theoretical curves, especially in the  $dI/dV$  are much sharper than in the measurement data is probably mainly due to the finite temperature  $T > 0$  and partly maybe also caused by smoothing the data which leads to a broadening of the features in the *IV*-curve.

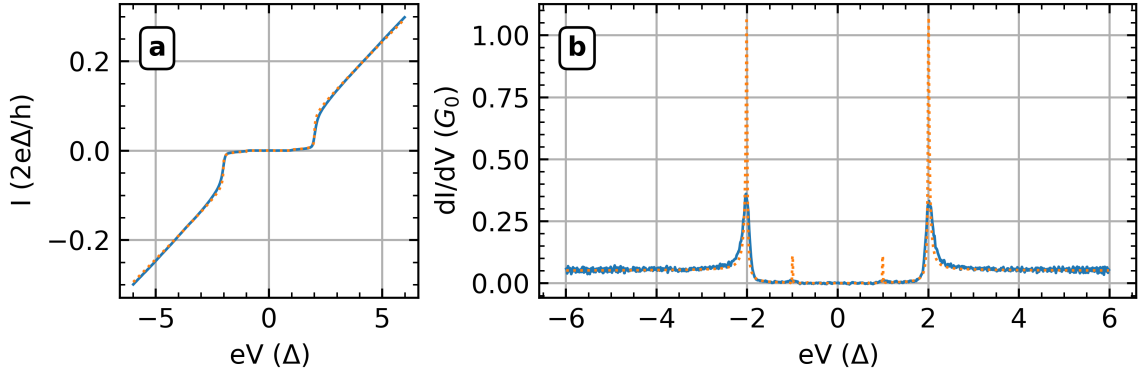


**Figure 4.9:** The PIN code analysis of the tunnel contact with a total conductance of  $G = 0.05 G_0$  finds one single transport channel with a transmission of  $\tau = 0.05$ . (a) shows the measured *IV*-curve as a solid line in blue and the fit as a dashed line in orange, (b) the  $dI/dV$ -curve calculated from (a) highlights the tunnel current at the gap edges and the remainders of ANDREEV reflections.

As basically only quasi-particle tunneling contributes to the electronic transport, this makes the tunnel contact especially suitable to start the analysis of microwave effects. The only features we expect are steps in the *IV*-curves around the gap edges caused by PAT. Figure 4.10 shows a frequency study of the tunnel contact. Voltage is applied on the x-axis, frequencies range up to 20 GHz on the y-axis and for every *IV*-curve we measured at each frequency, the calculated differential conductance is shown on the color bar. Without microwaves, there is no electronic transport possible for bias voltages below the gap voltage  $V = 2\Delta/e = 376 \mu\text{V}$ . With increasing microwave frequency the peaks in the  $dI/dV$  from the PAT fan out from the gap voltage. Superimposed on that, there are cavity effects which modulate the PAT.

If we now choose one frequency and vary the output power of the VNA instead of the microwave frequency, we arrive at the power study, that has already been shown

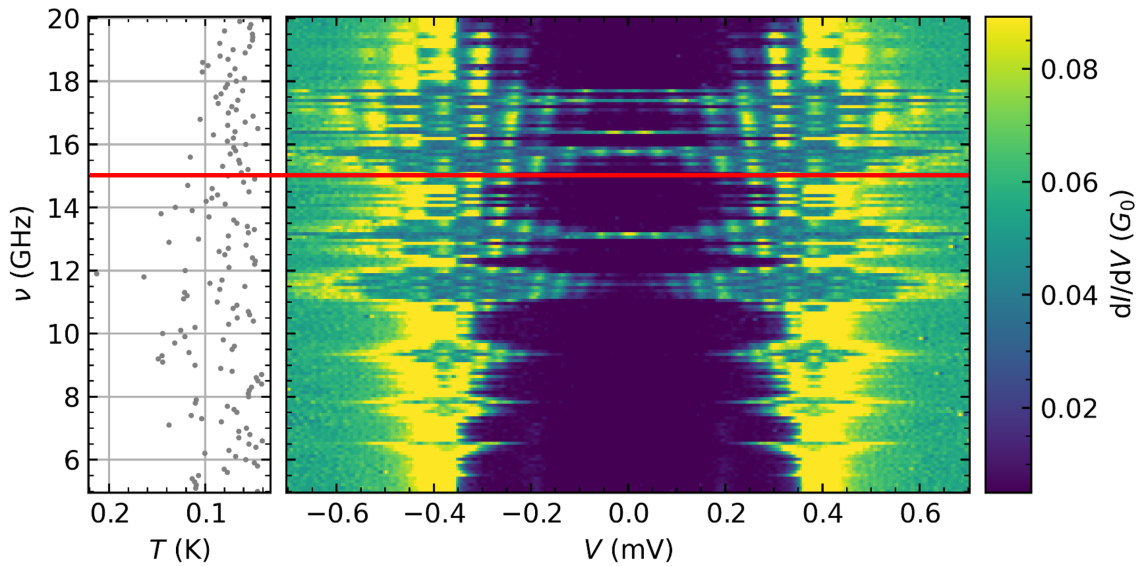


**Figure 4.10:** Frequency study at a microwave power of  $-20\text{ dBm}$  showing steps in the  $IV$ -curves caused by PAT as peaks in the differential conductance. The replicas of the peaks at the gap edges are modulated by cavity effects of the microwaves in the setup, this can be also seen in the temperature plot next to the color map. The horizontal red line indicates the frequency of  $15\text{ GHz}$ , where the power study was performed. The transmission of the contact is  $\tau = 0.05$ ,  $G = 0.05 G_0$ .

in figure 4.8 for explaining the linearization of the power axis. This power study was performed at a frequency of  $15\text{ GHz}$ . The tunnel contact can be fully understood within the TIEN-GORDON model presented in equation 2.16. Often the argument of the BESSEL function  $J_n^2\left(\frac{eV_\omega}{\hbar\omega}\right)$  is defined as  $\alpha = \frac{eV_\omega}{\hbar\omega}$ . This makes perfect sense when looking at single  $IV$ -curves, when looking at an entire color map, however, one can only define a proportionality constant which relates the output voltage  $V_{\text{out}}$  of the VNA to the local voltage amplitude  $V_\omega = \gamma \cdot V_{\text{out}}$ . The factor  $\gamma$  acts like a damping constant and is typically around  $0.01 = -20\text{ dB}$  which is reasonable for the expected damping coming from the cabling.

Using the TIEN-GORDON model it is possible to simulate the measurement based on an  $IV$ -curve in absence of microwave irradiation. All we need to do to achieve this is to shift the current  $I_0(V_0)$  by a voltage of  $n\hbar\omega/e$  for every order of PAT, that we want to include and weight it with the BESSEL function  $J_n^2\left(\frac{e\gamma V_{\text{out}}}{\hbar\omega}\right)$  of the corresponding order. The zeroth order is the peak in the differential conductance at  $\pm 2\Delta$ , the order of  $n = \pm 1$  are the peaks left and right with respect to the zeroth order peak in the differential conductance, and so on. In principle, it should not matter if we first shift and add the individual current contributions and then calculate the differential conductance  $dI/dV$  or if we first differentiate the  $IV$ -curve and then shift and add the  $dI/dV$ -curves. For technical reasons we are doing the latter as artifacts from the differentiation can be compensated more easily this way. Figure 4.11 shows the comparison of (a) experiment and (b) the simulation based on  $I_0$ , the tunnel current in absence of microwave irradiation.

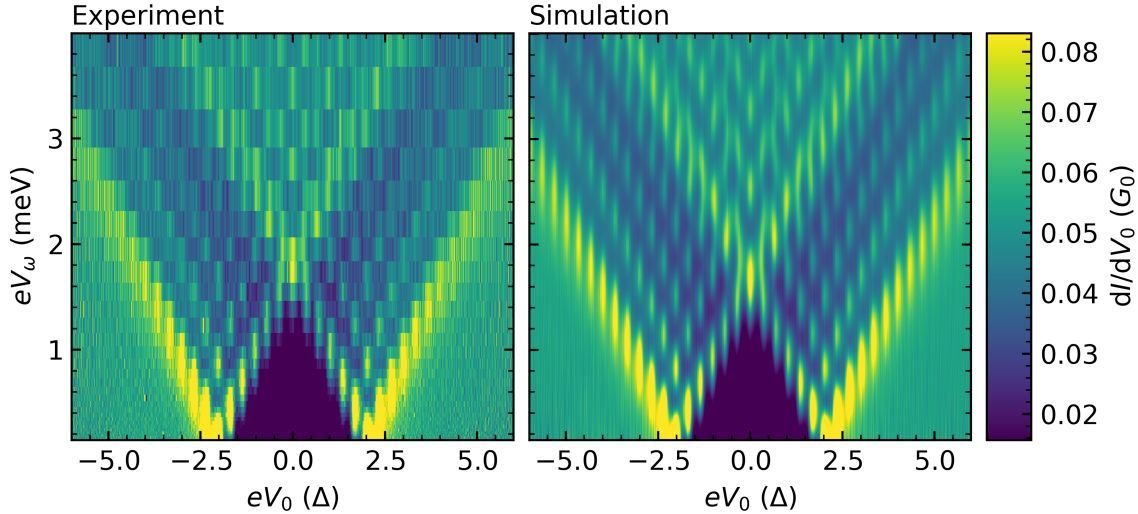


**Figure 4.11:** Power study comparing the experimental data with a simulation based on a  $dI/dV$ -curve in the absence of microwave irradiation. The transmission of the contact is  $\tau = 0.05$ ,  $G = 0.05 G_0$ . The microwaves have been coupled in via the stripline and their frequency was fixed to  $\nu = 15 \text{ GHz}$ . From minimizing the MSD of the two maps we find for the damping parameter  $\gamma = \frac{V_\omega}{V_{\text{out}}} = 0.0146$ . The simulation produces replicas of the peaks at the gap edges and modulates them according to the TIEN-GORDON equation.

The simulation can fully account for all features in the measured color map. It is remarkable how well this simple model agrees with the actual effects of increasing the microwave power. The V-shaped fans overlap around zero bias and form a complex interference pattern both for the experiment and the simulation. To achieve this good agreement we have run several simulations for different values of  $\gamma$  and calculated the mean squared deviation (MSD) of the entire color maps from simulation and experimental data, that were weighted with the point density. This is equivalent to a fit with  $\gamma$  as the only free parameter. For a value of  $\gamma = 0.0146$  we find a clear minimum in the MSD, which is shown in figure 4.12. If  $\gamma$  was chosen too small or too large, the periodicity of the BESSEL functions, that alternate in y-direction, would not match the experimental data and the slopes of the V-shaped fans would be different. The damping parameter  $\gamma$  will be recalculated for every map and shows slight deviations depending on whether the antenna or stripline is used. Of course,  $\gamma$  also changes with the applied microwave frequency.

In addition to simulating the color map based on a measured  $IV$ -curve in absence of microwave irradiation, it is also possible to base the simulation on the theoretical  $IV$ -curve that was obtained from the PIN code determination. For the tunnel contact this works very well as the theoretical curve fits nicely the measured data as shown in figure 6.3 in the appendix. This will no longer be the case for higher transmissions which have a non-negligible supercurrent. Unfortunately, the theory curves do not include the supercurrent at zero bias which means the simulation based on the theory curves cannot account for SHAPIRO steps. Apart from the fact that it produces

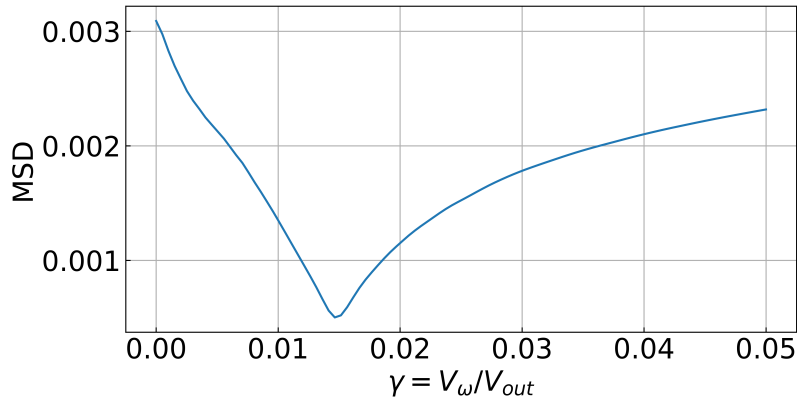


**Figure 4.12:** The damping parameter  $\gamma = \frac{V_\omega}{V_{out}}$  is determined by finding the minimum of the MSD of the color maps from the experimental data and the simulation. For the tunnel contact with a transmission of  $\tau = 0.05$ ,  $G = 0.05 G_0$  we find  $\gamma = 0.0146$ .

very sharp features, the simulation based on a theory curve does not provide any new insights compared to the simulation based on measured *IV*-curves in absence of microwave irradiation.

#### 4.2.2 Atomic Contact with Low Transmission

Atomic contacts in the range of few conductance quanta can have very different distributions of transmissions. The contact analyzed in this subchapter is the one with a total conductance of  $1.97 G_0$  already presented in figure 6.2b. While the supercurrent is not visible in the magnetic field study, the  $dI/dV$ -curve in figure 4.13 clearly shows a peak at zero bias. The fitting of the *IV*-curve finds six transport channels with the transmissions  $\tau_i = [0.25, 0.25, 0.25, 0.275, 0.35, 0.5]$ . The leading transmission is still moderate, yet significantly higher than for the tunnel contact, which means we expect to see additional features to the PAT we already know. This is what the experiments confirm: when irradiated with microwaves, replicas of the supercurrent show up as depicted in the frequency study in figure 4.14 and in the power study in figure 4.15.

As the microwaves are turned on, higher orders of MAR vanish and the supercurrent gets rather weak. However, the frequency study in figure 4.14 shows both, PAT and SHAPIRO steps (spikes in the  $dI/dV$ ) which can be differentiated by their position and the spacing of the lines. PAT takes place at the gap edges, whereas SHAPIRO steps fan out around zero bias. The SHAPIRO steps have half the spacing of the steps caused by PAT, this can be explained by the factor of  $2e$  in the denominator of equation 2.14. We have  $2e$  here as the charge carriers involved in this tunneling process are COOPER pairs. For the PAT it is only a factor of  $e$  as the charge carriers are quasi-particles. Furthermore, the SHAPIRO steps are much sharper than the PAT steps, as they only resemble the sharpness of quasi-particle tunneling onset at the gap voltage.

The supercurrent, which cannot be neglected anymore, makes the simulation more complicated. We have chosen to approach the simulation divided in two parts. First,

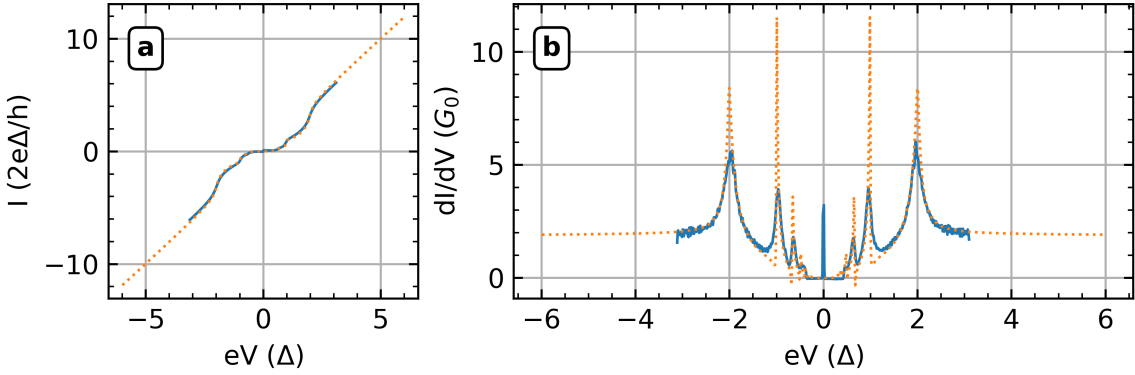


**Figure 4.13:** The PIN code analysis of the atomic contact with a total conductance of  $G = 1.97 G_0$  reveals six transport channels with the individual transmissions of  $\tau_i = [0.25, 0.25, 0.25, 0.275, 0.35, 0.5]$ . (a) shows the measured  $IV$ -curve in blue and the fit as a dashed line in orange, (b) the  $dI/dV$ -curve calculated from (a) highlights the supercurrent at zero bias and MAR up to the order  $m = 4$ .

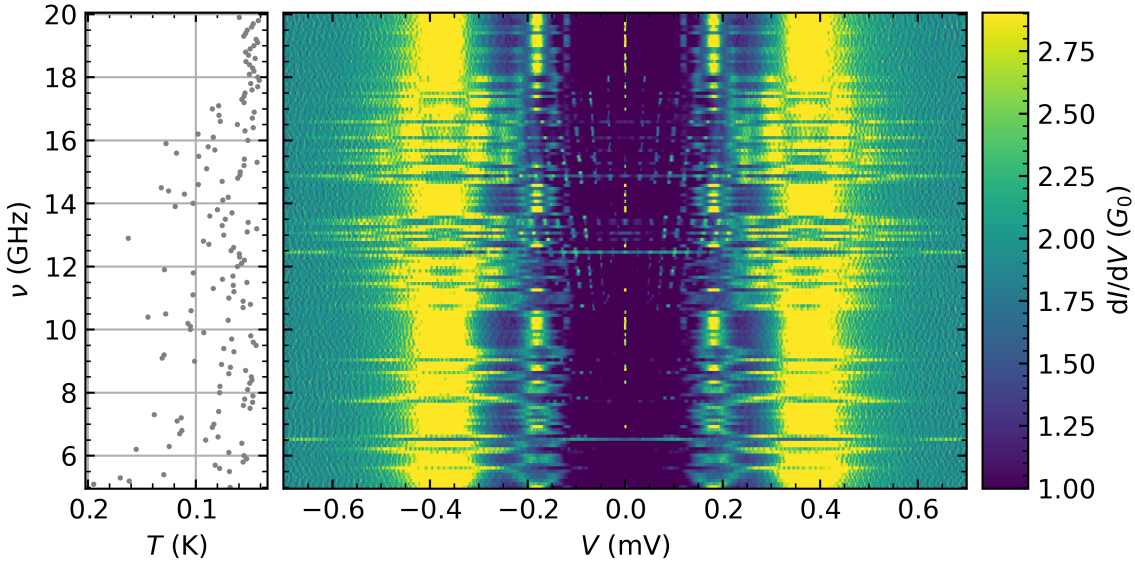


**Figure 4.14:** Frequency study at a microwave power of  $-25$  dBm showing PAT and SHAPIRO steps as peaks in the differential conductance. The individual channel transmissions are  $\tau_i = [0.25, 0.25, 0.25, 0.275, 0.35, 0.5]$ ,  $G = 1.97 G_0$ . As expected the SHAPIRO steps are much sharper than the ones from PAT and show half the spacing as expected from theory. As this contact only has low transmissions and a weak supercurrent, SHAPIRO steps and higher-order transport processes are only weakly pronounced.

we handle the PAT by manually excluding the supercurrent peak from the  $dI/dV$ -curve and then proceeding as described before. Second, we shift and replicate the previously excluded supercurrent according to equation 2.19 using the measured supercurrent peak, and third, we sum both parts to obtain the total differential conductance. The result of this is shown in figure 4.15 and reproduces the PAT and SHAPIRO steps with good agreement between simulation and experimental data. The damping parameter  $\gamma = 0.0136$  obtained from minimizing the MSD is comparable to what we found before even though we used the antenna for microwave irradiation in this measurement and not the stripline. Notice, that equation 2.19 is not what one would expect for SHAPIRO steps, but rather a modified version of the TIEN-GORDON equation where the quasi-particle's charge  $e$  has been replaced by  $2e$  for COOPER pairs. This fact will be discussed in detail in the next subchapter as for the following atomic contact with even higher transmission the SHAPIRO steps become more pronounced. In addition, also MAR of higher orders get more visible as well as the PAT of them. Here another discrepancy between experiment and simulation becomes apparent: the PAMAR is not correctly replicated by our current model for the simulations. When comparing the area around  $V = 1\Delta$  for experiment and simulation, one can see a weak fan starting from the ANDREEV reflection at  $\Delta$  with half the spacing of the PAT at  $2\Delta$  in the experiment. In the simulation, however, the fan is absent. This inconsistency will be discussed in more detail with the next atomic contact as the larger transmission amplifies the issue.

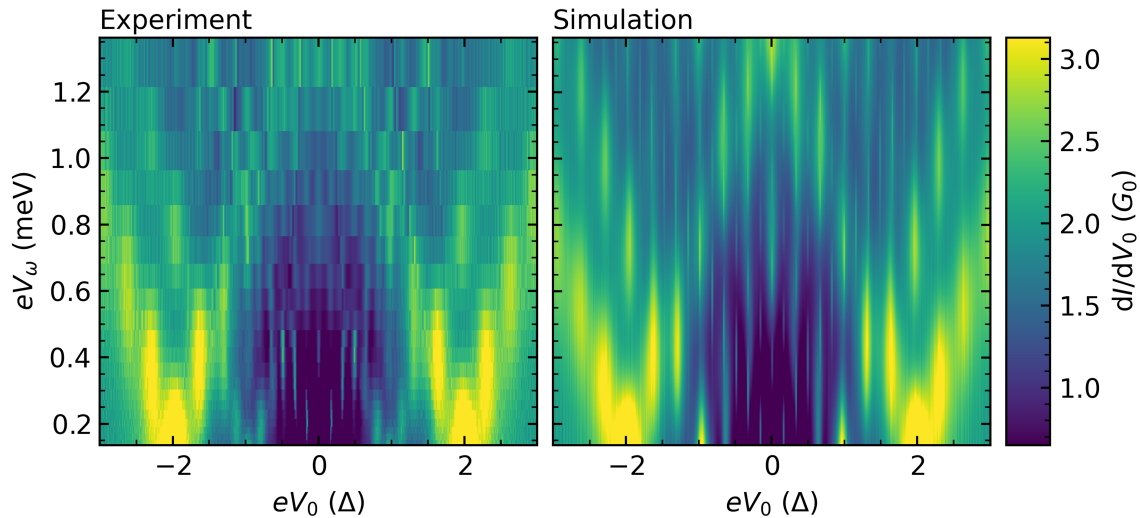


**Figure 4.15:** Power study comparing the experimental data with a simulation based on a  $dI/dV$ -curve in the absence of microwave irradiation. The individual channel transmissions are  $\tau_i = [0.25, 0.25, 0.25, 0.275, 0.35, 0.5]$ ,  $G = 1.97 G_0$ . The microwaves have been coupled in via the antenna and their frequency was fixed to  $\nu = 15$  GHz. From minimizing the MSD of the two maps we find for the damping parameter  $\gamma = \frac{V_\omega}{V_{\text{out}}} = 0.0136$ . The simulation sums up the contributions from PAT with the replicas of the supercurrent peak from the modified TIEN-GORDON equation.

### 4.2.3 Atomic Contact with High Transmission

For increasing transmissions, the *IV*-curves transition from a concave shape to a convex shape as illustrated in figure 2.4 in the theory chapter. This way, we can recognize at first glance that the contact with a total conductance of  $2.09 G_0$ , shown in figure 4.16, contains a transport channel with high transmission. The analysis of the PIN code for this atomic contact unveils a total of five transport channels with transmissions  $\tau_i = [0.01, 0.25, 0.325, 0.62, 0.8]$ . The  $dI/dV$ -curve in figure 4.16 even shows MAR up to the order  $m = 4$  which could not be resolved in the magnetic field study of this contact already shown in figure 6.2a.

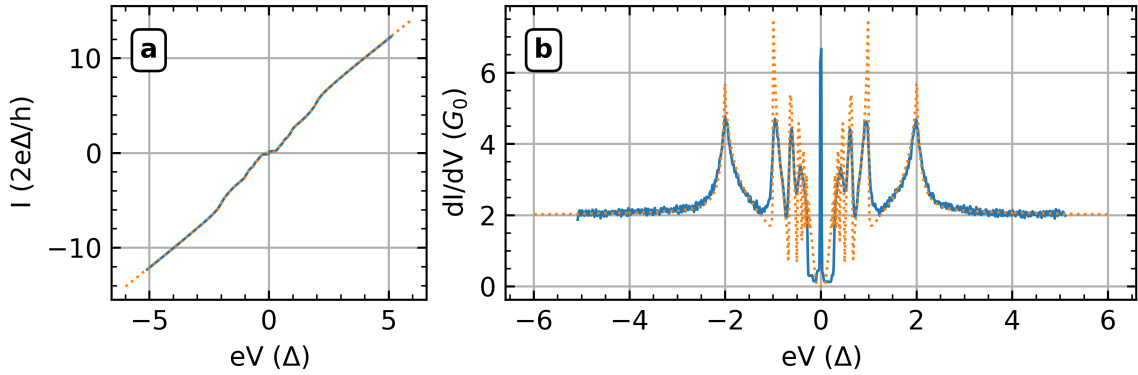


**Figure 4.16:** The PIN code analysis of the atomic contact with a total conductance of  $G = 2.09 G_0$  reveals five transport channels with the individual transmissions of  $\tau_i = [0.01, 0.25, 0.325, 0.62, 0.8]$ . (a) shows the measured *IV*-curve in blue and the fit as a dashed line in orange, (b) the  $dI/dV$ -curve calculated from (a) highlights the supercurrent at zero bias and MAR up to the order  $m = 4$ .

The strong supercurrent leads to a rich pattern of PAT and SHAPIRO steps which can be seen in the frequency study in figure 4.17. The reason why we can see more steps here than in figure 4.14 for the previous contact is simply the difference in microwave power. This frequency study was measured at a power of  $-20$  dBm, while the previous one was measured at a power of  $-25$  dBm. Distinguishing PAT and SHAPIRO steps is easy close to the gap edges and close to zero bias, the sharpness of the peaks and their spacing clearly distinguish them from each other. This gets more difficult when the two types of steps start to overlap. Things get even more complicated when fractional SHAPIRO steps show up which is expected of deviations from the sinusoidal current-phase relation caused by high transmissions. For frequencies around 19 GHz and for small bias voltages we can clearly see spikes that correspond to non-integer SHAPIRO steps. They will be investigated in a power study at 19.3 GHz shown in figure 4.21 in more detail.

So far I have always been talking about SHAPIRO steps when referring to the replicas of the supercurrent caused by microwave irradiation. However, it is arguable whether the replicas should really be called SHAPIRO steps. One reason not to call them SHAPIRO steps is the lack of functional relationship. As mentioned before in chapter , the simulation for the replicas of the supercurrent peak is based on a

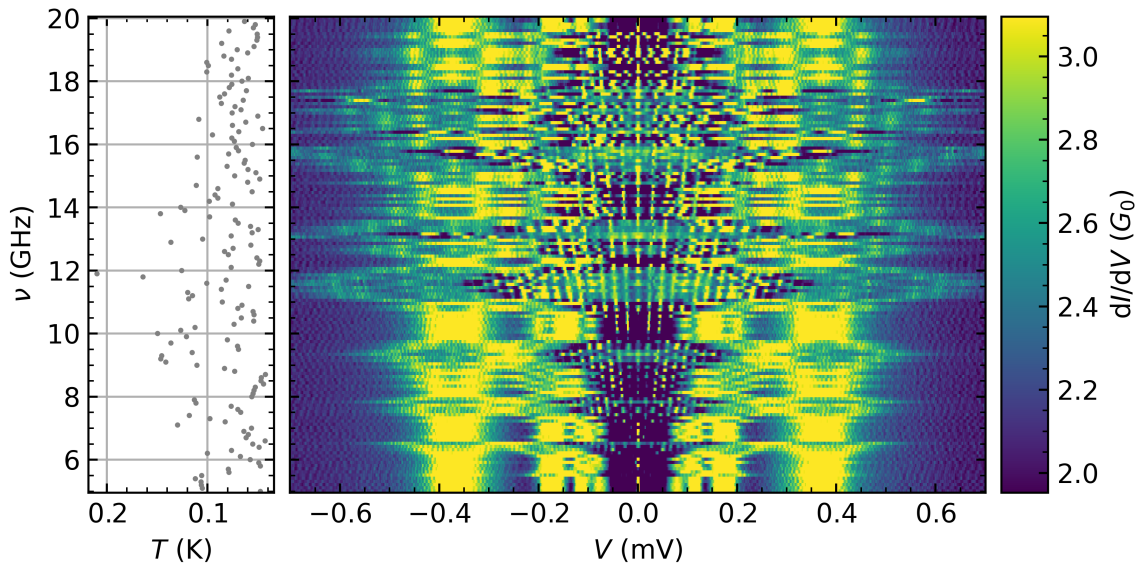


**Figure 4.17:** Frequency study at a microwave power of  $-20$  dBm showing many PAT and SHAPIRO steps in form of peaks in the differential conductance. PAT and SHAPIRO steps start to overlap for higher frequencies and for frequencies around  $19$  GHz even fractional SHAPIRO steps show up. The individual channel transmissions for this atomic contact are  $\tau_i = [0.01, 0.25, 0.325, 0.62, 0.8]$ ,  $G = 2.09 G_0$ .

modified version of the TIEN-GORDON equation where the quasi-particle's charge  $e$  has been replaced by  $2e$  for COOPER pairs. The main difference of the modified TIEN-GORDON equation to the equation describing SHAPIRO steps is the fact, that the BESSEL function is squared here, whereas this is not the case in equation 2.13 for the SHAPIRO steps. The periodicity of  $J_n$  and  $J_n^2$  is identical, but the amplitude of the squared BESSEL function is clearly smaller as the maximum amplitude of BESSEL function from the first kind  $J_n$  is 1 and squaring a number that is smaller than 1 makes it even smaller. The following two figures show a comparison of experimental data and simulation for implementing the BESSEL function without squaring it, as one would expect it for textbook SHAPIRO steps (figure 4.18), and with the BESSEL function squared, as proposed in the modified TIEN-GORDON equation (figure 4.19).

Comparing the two above figures, one can clearly see that the BESSEL function in figure 4.18 strongly overestimates the amplitude of the SHAPIRO steps, while the squared BESSEL function from the modified TIEN-GORDON equation in figure 4.19 fits the amplitude of the SHAPIRO steps quite well. The damping parameter  $\gamma = 0.0051$  which is recalculated for every simulation is smaller than before as the frequency used here is significantly smaller than for the previous power studies. Due to the zoom on small bias voltages and small amplitudes, the resolution in the experimental data makes it hard to exactly align the peaks of experiment and simulation in the color maps one by one. However, the modified TIEN-GORDON equation with the squared BESSEL function fits the experimental data much better.

Our results are consistent with the findings reported in the literature on low-temperature STM experiments [30, 40, 45] presented in chapter 2.8. To a certain

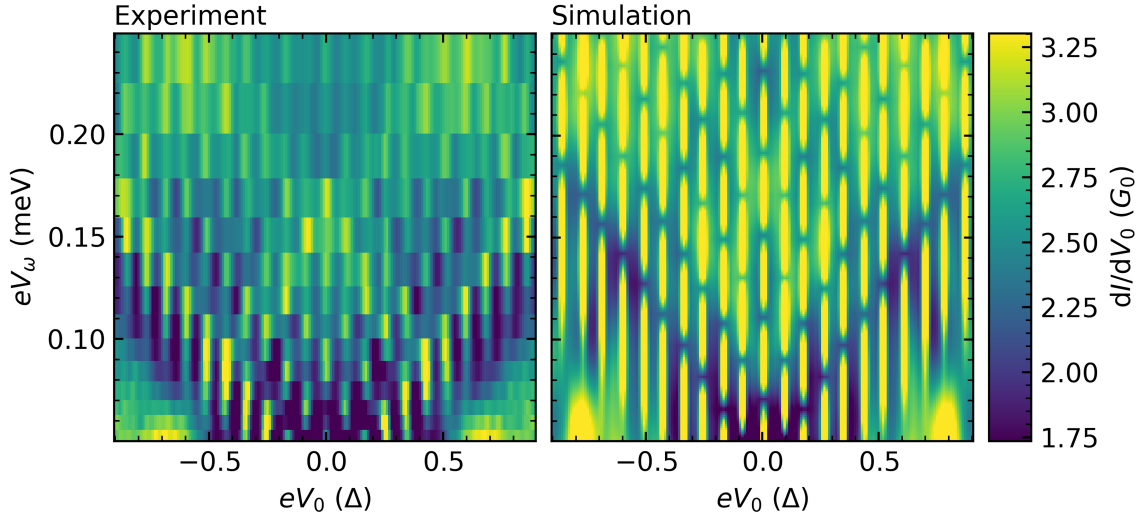


**Figure 4.18:** Power study comparing the experimental data from a contact with high transmission with a simulation based on a  $dI/dV$ -curve in the absence of microwave irradiation. The microwaves have been coupled in via the antenna and their frequency was fixed to  $\nu = 7.8$  GHz. The individual channel transmissions are  $\tau_i = [0.01, 0.25, 0.325, 0.62, 0.8]$ ,  $G = 2.09 G_0$ . From minimizing the MSD of the two maps we find for the damping parameter  $\gamma = \frac{V_\omega}{V_{\text{out}}} = 0.0051$ . The simulation uses the original equation with  $J_n$  for the amplitude of the SHAPIRO steps.

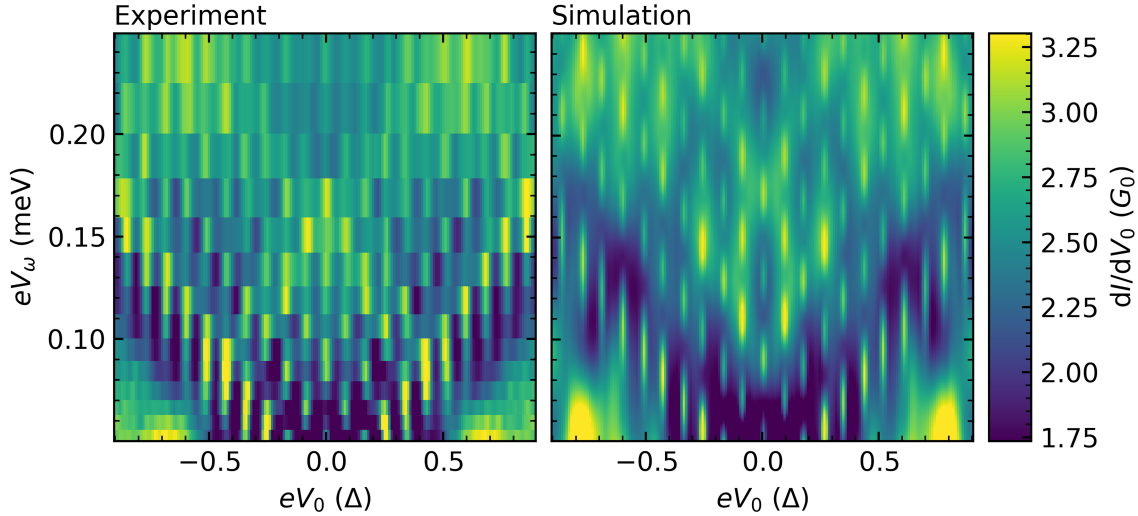


**Figure 4.19:** Power study comparing the experimental data from a contact with high transmission with a simulation based on a  $dI/dV$ -curve in the absence of microwave irradiation. The microwaves have been coupled in via the antenna and their frequency was fixed to  $\nu = 7.8$  GHz. The individual channel transmissions are  $\tau_i = [0.01, 0.25, 0.325, 0.62, 0.8]$ ,  $G = 2.09 G_0$ . From minimizing the MSD of the two maps we find for the damping parameter  $\gamma = \frac{V_\omega}{V_{\text{out}}} = 0.0051$ . The simulation uses the modified TIEN-GORDON equation with  $J_n^2$  for the SHAPIRO steps.

extent our MCBJ setup is similar to the atomic point contacts in STMs. It is the low capacitance (a high charging energy, respectively) of the junction that leads to the dynamical COULOMB blockade (DCB) effect and thus causes large phase fluctuations. As the sample was designed to investigate SETs, it was optimized to have high charging energies  $E_C$ . We can therefore assume, that we are far in the DCB regime and consequently have large quantum fluctuations of the phase and incoherent tunneling of Cooper pairs. That is a remarkable difference to the measurements performed by CHAUVIN *et al.* who successfully tweaked their aluminum-MCBJ setup towards a perfect voltage bias via an on-chip capacitor and resistor to minimize the phase fluctuations. As a consequence, the functional dependence of the intensity of the SHAPIRO steps is indeed described by a BESSEL function and not the square of BESSEL function as in the modified TIEN-GORDON model.

Not only the expression for the supercurrent requires modification to correctly reproduce the measurements in a simulation, also the TIEN-GORDON equation has to be generalized to properly capture PAMAR. A generalized TIEN-GORDON equation is presented in equation 2.18. This generalization is not implemented in the model we use in our simulations and is already the explanation for the deviations between the experimental data and the simulation, as already mentioned in the discussion of figure 4.15. To generate the simulated color map, we shift and add the entire  $dI/dV$ -curve (excluding the supercurrent peak at zero bias) to create the replicas of the gap edges. At the same time, we naturally also create replicas of the MAR peaks, but with an incorrect spacing on the voltage axis and the wrong periodicity of the BESSEL function as the order  $m$  of the MAR is not taken into account.

Figure 4.20 shows this issue even more clearly than in the previous example since for this atomic contact with a higher transmission the MAR are more pronounced. The  $dI/dV$ -curve without microwave irradiation, which is the starting point for the simulation, shows peaks at  $\pm 2\Delta$ ,  $\pm 1\Delta$  and  $\pm 2/3\Delta$ , which are then modulated and shifted incorrectly. On the one hand, one should keep in mind, that the y-axis does not start at zero microwave amplitude and that the zeroth peak of a the BESSEL function  $J_0^2(m\alpha)$  drops faster for increasing order  $m$  of the MAR. This means the zeroth peak has already dropped in the experiment while the simulation shows a broader peak at the positions  $\pm 2\Delta/m$ . The more intense peak slightly below  $1\Delta$  in the experimental data is a superposition of the zeroth peaks from  $J_{\pm 1}^2(m=2)$  and  $J_{\mp 1}^2(m=3)$  which finds no analog in the simulation. In the simulation on the other hand, there are two strong peaks around  $1.5\Delta$  at the same position on the y-axis, which is not the case for the experimental data, because the periodicity of the BESSEL functions depends on the order  $m$  of the MARs. All the points just mentioned provide evidence that PAMAR is sensitive to the number of charges involved in the process, which goes beyond the simple TIEN-GORDON model.

Implementing the generalized form of the TIEN-GORDON equation in the simulations is significantly more laborious if one wants to simulate the entire color map and not just sections of it, as CARRAD *et al.* [43] do for their nanowire JOSEPHSON junctions. This is something which might be done in future analysis.

For higher frequencies we have already seen in the frequency study in figure 4.17, that there are indications of fractional SHAPIRO steps. A power study performed at  $\nu = 19.3$  GHz provides more evidence for that. Figure 4.21 shows a zoom on the experimental data at small voltages around zero bias next to a simulation which includes half-integer SHAPIRO steps additionally to the simulation program used to produce the previous color maps with SHAPIRO steps. The fractional SHAPIRO steps use half-integer BESSEL functions  $J_q$  with  $q = \pm\frac{1}{2}, \pm\frac{3}{2}, \dots$  at positions exactly between two integer steps and weighted them with a factor of 0.4 with respect to the integer SHAPIRO steps, which was chosen by eye. In principle one would expect to see fractional SHAPIRO steps for fractions  $1/m$  with  $m$  being the order of a significant MAR [36]. As the  $IV$ -curve in figure 4.16 shows MARs up to the order of  $m = 4$  one would expect to see fractional SHAPIRO steps with denominators 2,3 and 4. On the other hand it is known, that fractional SHAPIRO steps are more sensitive temperature. This has been shown theoretically by DUPRAT *et al.* [57] and is confirmed by the experimental findings of CHAUVIN *et al.* [38]. For this reason, the weighting of the fractional SHAPIRO steps with a factor of 0.4 makes sense. Due to this increased temperature sensitivity higher fractional SHAPIRO steps might be suppressed strongly and therefore not visible in our measurements.

Just like for the previous simulations, the damping parameter  $\gamma = 0.0247$  was calculated via minimizing the MSD of the two color maps. As expected, we find a larger  $\gamma$  for the larger frequency. If we ignore the peak at  $\pm 2/3\Delta$  which comes from the incorrect implementation of the PAMAR in the simulation, the position and amplitude of the integer SHAPIRO steps can be reproduced quite well, especially up to order  $n = 2$ . The half-integer SHAPIRO steps, however, are curved towards the next higher integer SHAPIRO step. Additionally, there is a feature in the experimental data that starts at the end of an integer SHAPIRO step, (splits up in positive and negative bias in the case of the peaks belonging to the zeroth BESSEL function  $J_0$ ), and ends at the beginning of the next peak of the next order BESSEL function  $J_{\pm 1}$ .

So far there is no conclusive interpretation for these curved features. It is difficult to say whether only the half-integer SHAPIRO steps are curved and the diagonal lines are another additional feature, or whether the integer SHAPIRO steps are curved and the fractional SHAPIRO steps only replicate this curving of the integer SHAPIRO steps. If it is only the fractional SHAPIRO steps that are curved, one possible explanation would be that there are somehow higher orders of subharmonic SHAPIRO steps that cannot be resolved individually. Since the following two atomic contacts also show no signs of further fractional SHAPIRO steps, I rather believe that the integer SHAPIRO steps themselves are already curved and the fractional SHAPIRO steps only resemble that shape. Technically speaking, we do not have SHAPIRO steps, but incoherent tunneling of COOPER pairs which is rather related to PAT and PAMAR. The "SHAPIRO steps" we observe therefore only replicate the supercurrent just as PAT replicates the quasi-particle tunneling current onset at the gap edges. This means that if the supercurrent peak is curved in a way, one can also expect that its replicas are curved in the same way as well. The reason why the integer SHAPIRO steps would be curved in the first place remains unknown.

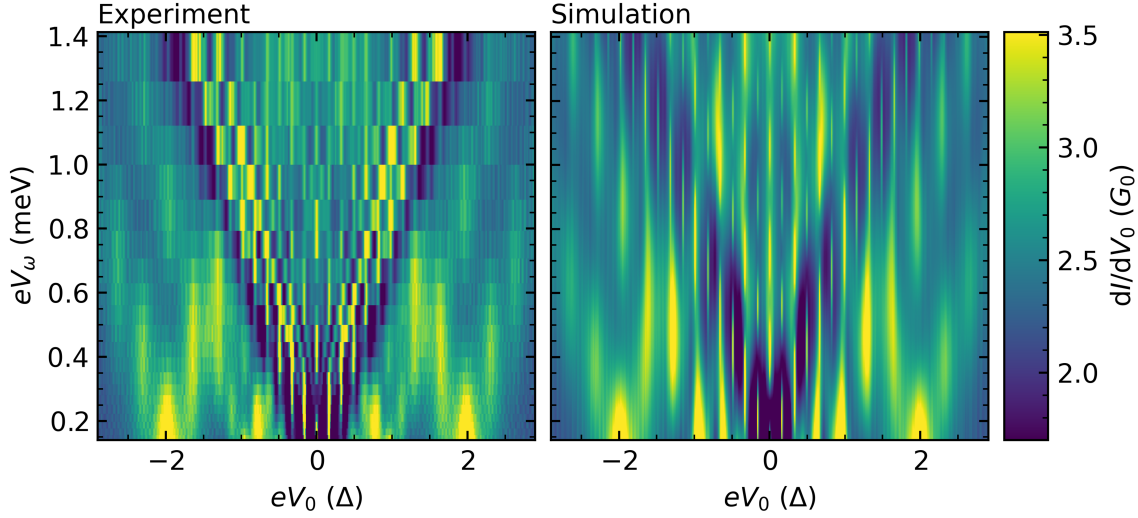


**Figure 4.20:** Power study comparing the experimental and simulation. The microwaves have been coupled in via the antenna and their frequency was fixed to  $\nu = 15$  GHz. The individual channel transmissions are  $\tau_i = [0.01, 0.25, 0.325, 0.62, 0.8]$ ,  $G = 2.09 G_0$ . From minimizing the MSD of the two color maps we find for the damping parameter  $\gamma = \frac{V_\omega}{V_{\text{out}}} = 0.0141$ . The simulation uses the modified TIEN-GORDON equation with  $J_n^2$  for the SHAPIRO steps. The discrepancies between experiment and simulation show that PAMAR goes beyond the simple TIEN-GORDON model.

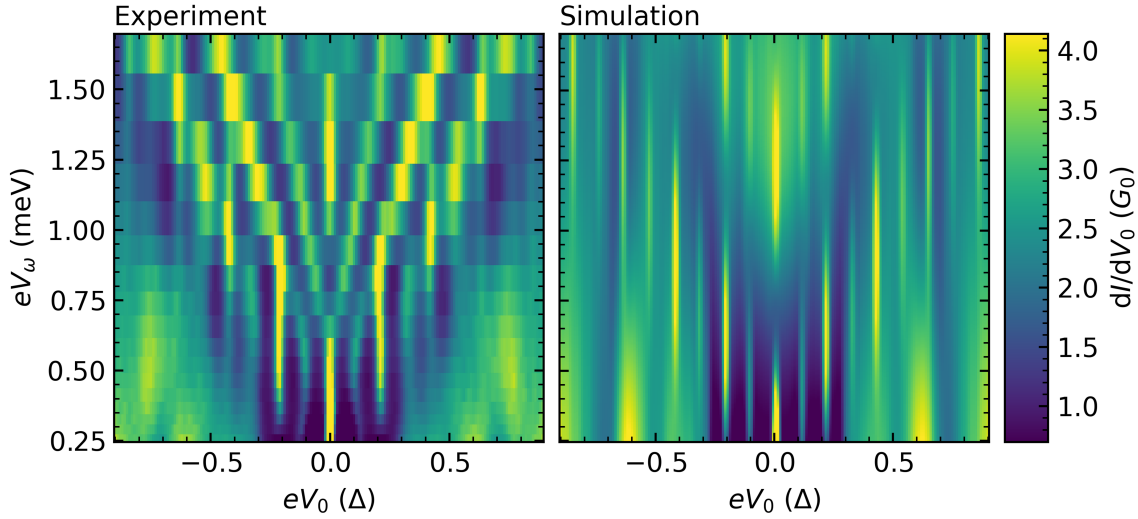


**Figure 4.21:** Comparison of experiment and simulation. The microwaves have been coupled in via the antenna and their frequency was fixed to  $\nu = 19.3$  GHz. The individual channel transmissions are  $\tau_i = [0.01, 0.25, 0.325, 0.62, 0.8]$ ,  $G = 2.09 G_0$ . From minimizing the MSD of the two color maps we find for the damping parameter  $\gamma = \frac{V_\omega}{V_{\text{out}}} = 0.0247$ . The simulation uses the modified TIEN-GORDON equation with  $J_n^2$  for the SHAPIRO steps. Additionally, half-integer SHAPIRO steps were implemented by placing them between two integer steps and weighting them with a factor of 0.4.

#### 4.2.4 Atomic Contact with Perfect Transmission

Finding an atomic contact with perfect transmission is possible in principle, but requires patience. We found multiple contacts with almost perfect transmission  $\tau = 0.99$ , one of which is presented in this subchapter. The best fit of the transmission finding algorithm could be achieved with a total conductance of  $G = 2.06 G_0$  and six transport channels with the transmissions  $\tau_i = [0.04, 0.15, 0.15, 0.15, 0.5, 0.99]$ . Even more than for the previous atomic contact which had a leading transmission of  $\tau = 0.8$ , this contact shows a very convexly shaped *IV*-curve as shown in figure 4.22a. The  $dI/dV$ -curve in figure 4.22b is clearly dominated by the steep current rise around zero bias. This strong peak is probably a combination of the supercurrent and MAR of very high order.

Just like the  $dI/dV$ -curve dominated by the zero-bias peak, the replicas of the zero-bias peak caused by the microwave irradiation dominate the frequency and power study for this atomic contact. The peaks at  $2\Delta/n$  are very small and broad compared to the zero-bias peak, this also causes pale replicas by PAT and PAMAR. It was very difficult to adjust the contrast in order to emphasize the other features except for the replicas of the zero-bias peak more strongly. This holds true for both the frequency study and the power study. Figure 4.23 shows the frequency study of this contact with almost perfect transmission. The PAT is pale, but clearly visible at the gap edges. Individual SHAPIRO steps and possibly fractional SHAPIRO steps are difficult to resolve, but one can anticipate that there are lines fanning out from zero bias with a spacing that corresponds to the known SHAPIRO steps. Since we suspect that MAR of very high order contributes to the peak at zero bias, we expect washed-out replicas, which only replicate the sharpness of the gap edges. This might explain why we cannot resolve the individual SHAPIRO steps.

The simulation of the power study shown in figure 4.24 accurately reproduces the PAT, yet it is not very convincing for the small bias voltages and the SHAPIRO steps. While the simulation generates many V-shaped features at zero bias nested inside each other, the experimental data only shows one V-shaped feature. I tried simulating with  $J_n^3$  and  $J_n^4$  instead of the squared Bessel function in order to let the amplitude of the peaks decrease faster, but the results were not convincing. The simulation only takes half-integer SHAPIRO steps into account and weights them with the same factor of 0.4 as before. For this almost perfect transmission the half-integer SHAPIRO steps are enough to fill the space between two integer steps. Therefore, this atomic contact does not provide us with any information as to whether there are other fractional SHAPIRO steps in addition to the half-integer SHAPIRO steps we already discussed before.

#### 4.2.5 Closed Contact with High Conductance

Once the MCBJ has been opened for the first time it is impossible to reach the initial state again. The measurements presented in this subchapter have been carried out in the attempt to fully close the MCBJ again. The result was a junction with a normal conductance of  $43.14 G_0$  which corresponds to a resistance of  $\sim 300 \Omega$ . Although there

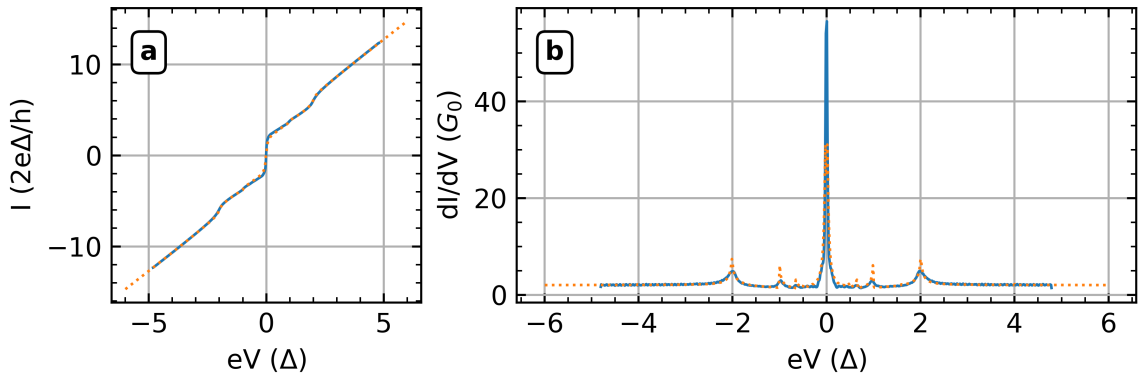


**Figure 4.22:** The PIN code analysis of the atomic contact with a total conductance of  $G = 2.06 G_0$  reveals six transport channels with the individual transmissions of  $\tau_i = [0.04, 0.15, 0.15, 0.15, 0.5, 0.99]$ . (a) shows the measured  $IV$ -curve in blue and the fit as a dashed line in orange, (b) the  $dI/dV$ -curve calculated from (a) highlights the strongly dominating steep current rise at zero bias and MAR up to the order of at least  $m = 4$ .

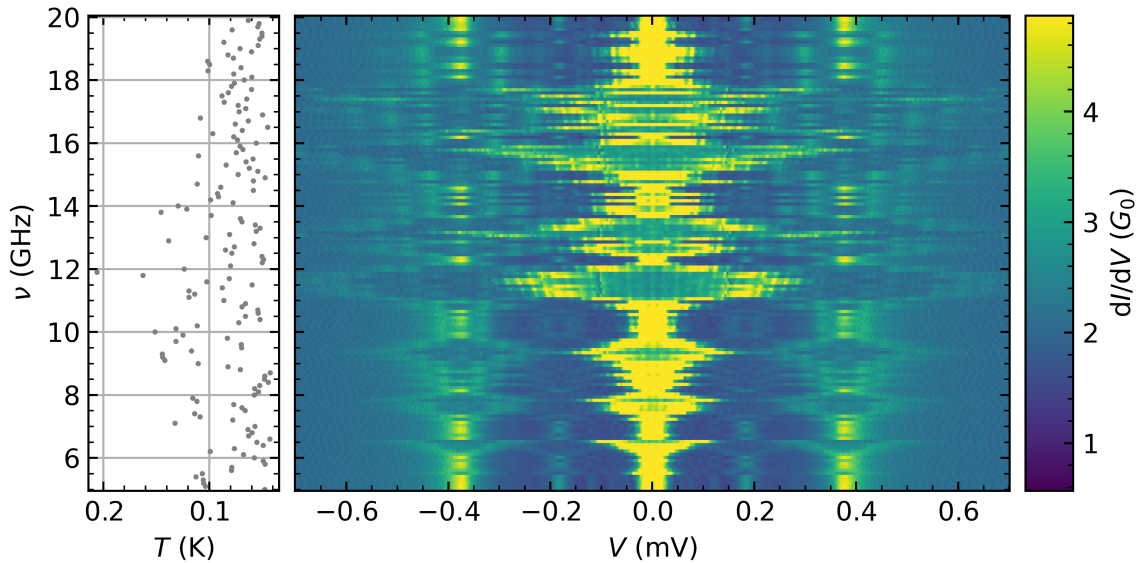


**Figure 4.23:** Frequency study at a microwave power of  $-20$  dBm showing PAT and SHAPIRO steps as peaks in the differential conductance. The individual channel transmissions of this contact are  $\tau_i = [0.04, 0.15, 0.15, 0.15, 0.5, 0.99]$ ,  $G = 2.06 G_0$ . The replicas of the supercurrent clearly dominate the color map and make it hard to see PAT or even PAMAR. Integer SHAPIRO steps are accompanied by fractional SHAPIRO steps that are difficult to resolve.

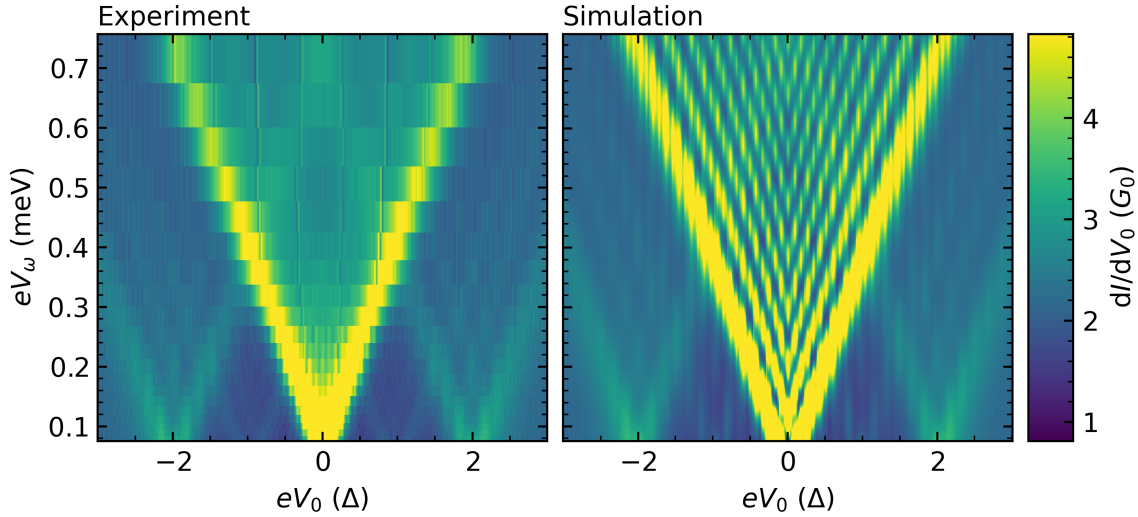


**Figure 4.24:** Power study comparing the experimental data from an atomic contact with almost perfect transmission with a simulation based on a  $dI/dV$ -curve in the absence of microwave irradiation. The microwaves have been coupled in via the stripline and their frequency was fixed to  $\nu = 7.8 \text{ GHz}$ . The individual channel transmissions are  $\tau_i = [0.04, 0.15, 0.15, 0.15, 0.5, 0.99]$ ,  $G = 2.06 G_0$ . From minimizing the MSD of the two maps we find for the damping parameter  $\gamma = \frac{V_\omega}{V_{\text{out}}} = 0.0076$ . The simulation uses the modified TIEN-GORDON equation with  $J_n^2$  for the integer and half-integer SHAPIRO steps, where the fractionals are weighted with a factor of 0.4.

is only an order of magnitude difference to the virgin state sample (never opened MCBJ) the measurements under microwave irradiation show fundamentally different results. Here, we observe the behavior of a ballistic conductor manifested through distinct conduction channels, whereas for the virgin state ("low-Ohmic contacts") sample we see the properties of a macroscopic diffusive superconductor with two critical currents for different parts of the sample that turn normal conducting. A lower estimate for the number of atoms is that at least 15 aluminum atoms form the junction as one aluminum atom can contribute with up to three conduction channels to the electronic transport and the normal conductance divided by three is larger than 14. This is only a lower estimate, as the number of channels per atom that contribute to the electronic transport decreases for larger contacts. The analysis of the PIN code of this contact to determine the individual transmissions of the contributing channels was not possible due to the vast number of required conduction channels. The maximum conductance that the transmission finding algorithm can account for would be  $6 G_0$  with six perfectly transmitting channels as the total number of channels included in the model for the PIN code analysis is six channels.

Unlike the low-Ohmic contacts, this highly conductive junction shows a strong response to microwave irradiation displaying many orders of SHAPIRO steps as shown in figure 4.25. For very low frequencies one can basically see a  $dI/dV$ -curve in the absence of microwave irradiation. There are MAR visible up to the order of  $m = 4$ , where especially the fourth order is pronounced. For reasons I do not understand,

there is no higher orders of MAR visible, but instead an area of low conductance that is only overlapped by the SHAPIRO steps fanning out from zero bias. Compared to the SHAPIRO steps, the PAT is almost invisible, but there are half-integer SHAPIRO steps clearly visible in between the integer SHAPIRO steps for frequencies of  $\sim 15$  GHz and higher.

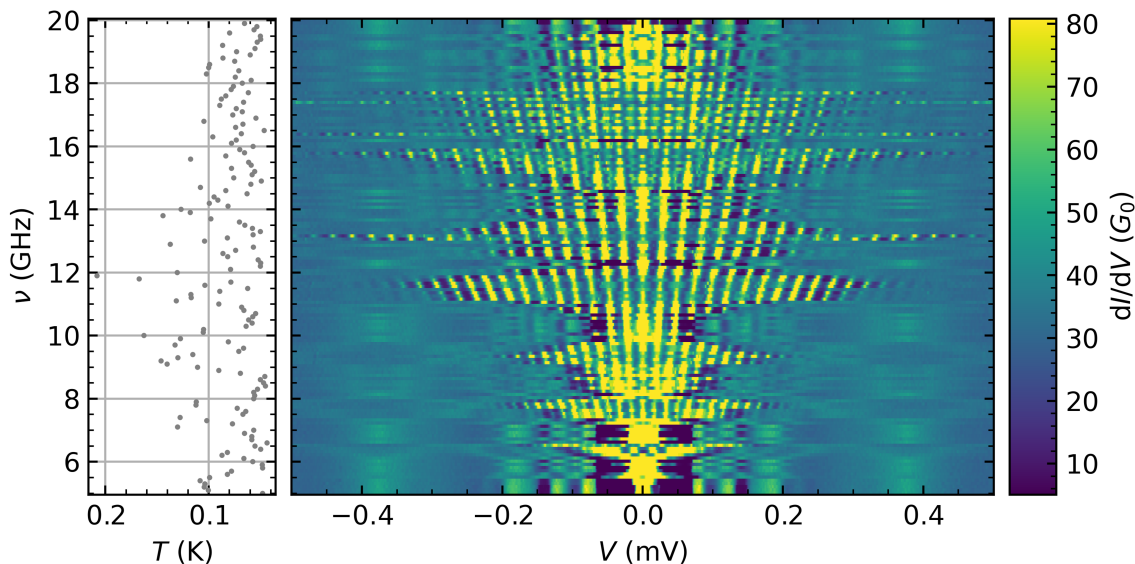


**Figure 4.25:** Frequency study for a highly conductive contact with conductance of  $43.14 G_0$  at a microwave power of  $-20$  dBm showing SHAPIRO steps and some remainders of PAT as peaks in the differential conductance. For higher frequencies half-integer SHAPIRO steps clearly get visible in between the integer SHAPIRO steps.

Both, the PAT and the (fractional) SHAPIRO steps can be observed even better in the power study presented in figure 4.26 for a frequency of 15 GHz. Although the fractional SHAPIRO steps are more pronounced and the spacing on the voltage axis would be larger, I chose to present the power study at 15 GHz instead of the one we carried out at 19.3 GHz, as due to an error in the code of the measurement program we did not cover the full range of output powers for the higher frequencies. This power study, however, shows excellent agreement of experiment and simulation within the uncertainty due to the pixel height. The damping parameter  $\gamma = 0.0197$  was obtained by minimizing the MSD of the two maps and the half-integer SHAPIRO steps were weighted with a factor of 0.4. Compared to the contact shown in figure 4.21, the curving of the SHAPIRO steps and half-integer SHAPIRO steps is less intense, but especially for the half-integer SHAPIRO steps still present. The fact that we only observe half-integer SHAPIRO steps, yet no higher fractions could be due to the stronger temperature sensitivity of the fractional SHAPIRO steps as mentioned before.

Many sources on fractional SHAPIRO steps present color maps showing the differential resistance with the bias current instead of voltage on the x-axis [50–52]. The SHAPIRO steps which are peak-shaped in a single  $dI/dV$ -curve or line-shaped in the differential conductance map become lobe-shaped in this other representation, which

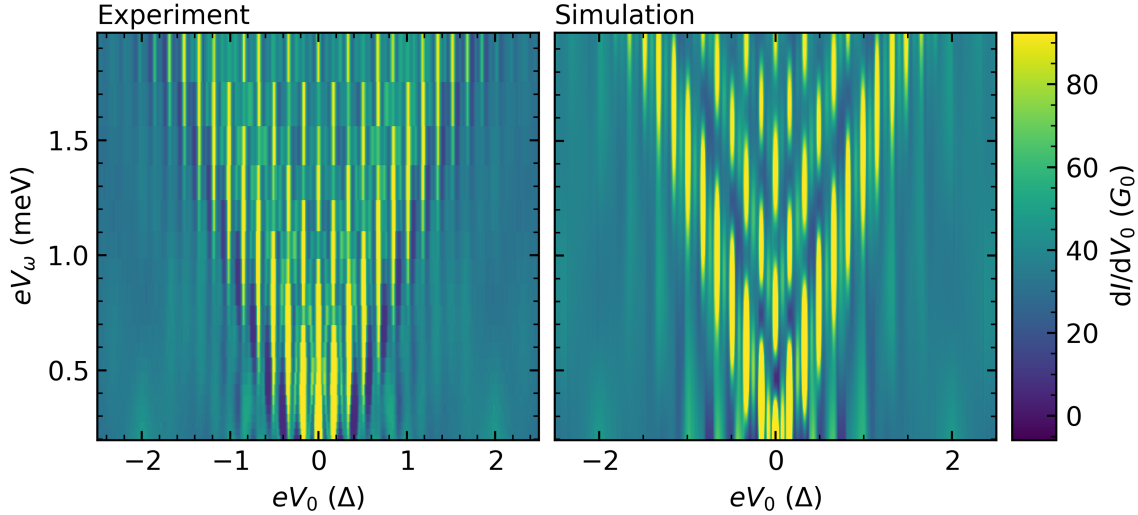


**Figure 4.26:** Power study comparing the experimental data of a re-closed contact with very high conductance of  $43.14 G_0$  with a simulation based on a  $dI/dV$ -curve in the absence of microwave irradiation. The microwaves have been coupled in via the antenna and their frequency was fixed to  $\nu = 15$  GHz. From minimizing the MSD of the two maps we find for the damping parameter  $\gamma = \frac{V_\omega}{V_{\text{out}}} = 0.0197$ . The simulation uses the modified TIEN-GORDON equation with  $J_n^2$  for the integer and half-integer SHAPIRO steps, where the fractionals are weighted with a factor of 0.4.

makes it difficult for comparison. In a follow-up analysis, one could try to bring our data into the same format to facilitate a comparison of the results. Three interesting recent publications which use the SHAPIRO lobe representation are the ones already mentioned in chapter 2.8. These experiments on highly transmissive nanowires [50, 51] and nanoflags [52] show half-integer and no further fractional SHAPIRO steps as well. The work on nanoflag junctions reports that the half-integer SHAPIRO steps are robust to temperature. This would also be an interesting test for your system. Unfortunately we have not been able to control the temperature in our setup so far.

Despite having mostly used the term SHAPIRO steps for the replicas of the supercurrent under microwave irradiation, none of the atomic contacts discussed above is described by the equation for SHAPIRO steps. Instead, all replicas of supercurrent are caused by photon-assisted phase-incoherent tunneling of COOPER pairs which are described by an expression that is very similar to the TIEN-GORDON equation where the intensity of the steps is modulated by a squared Bessel function instead of the Bessel function itself. This is nothing new, has been well understood from a theoretical point [44] of view and has been observed in multiple experiments [30, 40, 43, 45]. However, to the best of my knowledge no one has yet reported half-integer steps for photon-assisted phase-incoherent tunneling of COOPER pairs or fractional steps in general. Our measurements have therefore not only been able to reproduce many known results, but also to find fractional steps for photon-assisted phase-incoherent

tunneling of COOPER pairs that cannot be understood within the framework of SHA-PIRO steps.

#### 4.2.6 Comparison of Antenna and stripline

In the previous chapters I have been mainly, but not exclusively showing measurement results of experiments using the antenna for microwave irradiation. The reason for this is that the results are very comparable and hardly show any differences. Upon closer inspection, small flaws become apparent, for example in figure 4.24a, which shows the power study for atomic contact with almost perfect transmission. Here, artifacts appear in the form of individual pixels at regular spacing, which become spaced further apart for greater power. The origin of these artifacts is unknown, but they only occur in the measurements with the stripline and not in the antenna. Figure 4.27 shows a direct comparison of the same measurement done with antenna and stripline. The measurement selected for this comparison is the power study at 15 GHz for the contact with a conductance of  $43.14 G_0$ , as the damping parameter  $\gamma$  was most similar here. The measurement with the stripline also shows the previously mentioned artifacts, in addition there is a horizontal line sticks out at  $-17 \text{ dBm}$ . It is difficult to tell, but it almost seems as if the artifacts only start above this line. Below this horizontal line the measurement data for antenna and stripline look identical, above the line the antenna shows somewhat sharper peaks and, in contrast to the stripline, no artifacts.

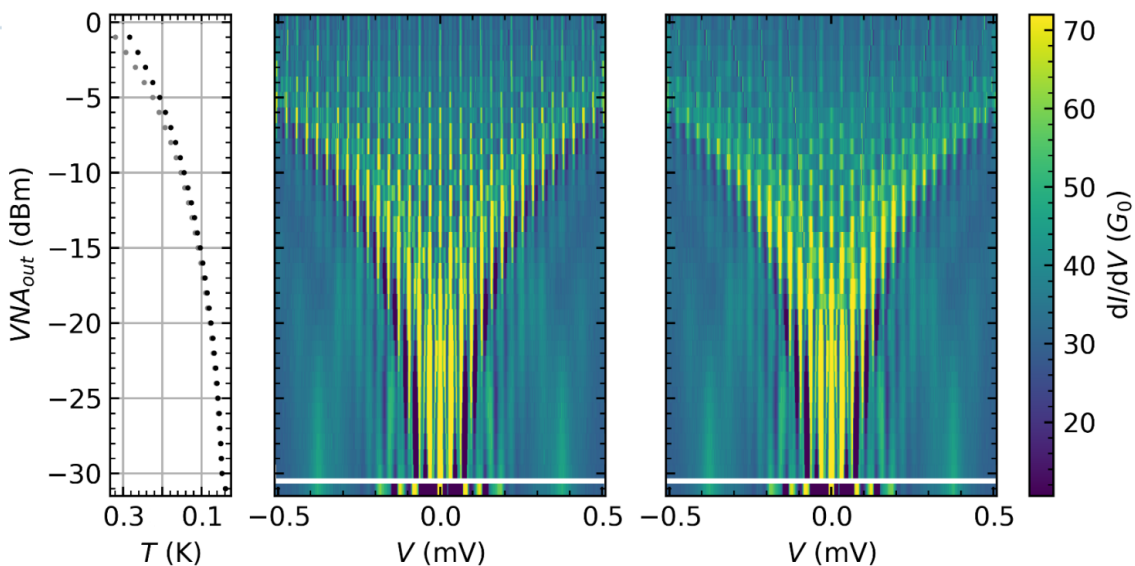


**Figure 4.27:** Power study comparing the experimental results from a measurement using (a) the antenna and (b) the stripline for microwave irradiation. The antenna seems to produce sharper features with less artifacts. The bottom row below the white line of both color maps shows a  $dI/dV$ -curve in measured the absence of microwave irradiation.

Despite the artifacts, we thought for a long time that the stripline would at least

provide more power and therefore greater local amplitudes, as planned in the initial considerations. A closer look at damping parameters  $\gamma = \frac{V_\omega}{V_{\text{out}}}$  for different measurements reveals a more mixed picture. Table 4.2 shows the damping parameters for a selection of atomic contacts. All values for  $\gamma$  were all obtained individually by minimizing the MSD of the color maps for experiment and simulation. Small values of  $\gamma$  mean a stronger attenuation and thus less local amplitude  $V_\omega$ . For better readability the values for  $\gamma$  are given in % here.

**Table 4.2:** Comparison of the microwave power damping parameter  $\gamma$  for antenna (first value) and stripline (second value). The first value always corresponds to the antenna, the second one to the stripline. The damping parameter is defined as the ratio between the local voltage amplitude and the output voltage of the VNA  $\gamma = \frac{V_\omega}{V_{\text{out}}}$ . All values for  $\gamma$  were obtained by minimizing the MSD of the color maps for experiment and simulation and are given in % here.

a vs. s	7.8 GHz	15 GHz	19.3 GHz
2.09 $G_0$	0.51 < 0.66	1.41 > 1.36	2.47 > 1.77
2.06 $G_0$	0.51 < 0.76	1.72 < 2.22	3.33 > 2.98
43.1 $G_0$	0.56 < 0.66	1.97 = 1.97	2.54 > 1.93
0.82 $G_0$	0.51 < 0.56	1.36 > 1.26	2.02 > 1.52

We usually performed power studies at three frequencies with antenna and stripline. Unfortunately, the tunnel contact, where the sample was bent the most, was only measured with the stripline at 15 GHz. This does not allow for any conclusions regarding the differences in power at different distances. However, the data presented here shows no trend for the different conductance values and thus no significant dependency of the microwave power emitted from the antenna for varying degrees of MCBJ opening. The situation is different with regard to frequencies. Here the stripline seems to generate larger local amplitudes at low frequencies, whereas the antenna does this at higher frequencies.

If I had to choose one option for microwave irradiation, I would opt for the antenna, as it produces slightly clearer color maps with no artifacts. Since it is not much effort to contact the stripline as well, I would recommend to continue using both methods for microwave irradiation in the future. The advantage here is that line-specific frequency dependencies of one microwave cable can be bypassed by the other without difficulty. Furthermore, a second microwave transmitter creates redundancy and can thus contribute towards successful experiments.

## 5 Conclusion and Outlook

In this master's thesis I have set up the microwave irradiation in order to induce a non-equilibrium in the MCBJ-SET in future measurements and thus trigger quantum fluctuations in a controlled manner, together with OLIVER IRTENKAUF. We simplified our sample design from an MCBJ-SET to a simple aluminum MCBJ to observe microwave effects on a JOSEPHSON junction in first test measurements to characterize the newly installed microwave cables. The simplification of the sample design was done in two steps whereby both types of simplified samples were analyzed in multiple magnetic field studies before opening the MCBJ for the first time. Both types of microwave transmitters, antenna and stripline, show the SHAPIRO steps we were expecting plus additional steps in the *IV*-curves we had not anticipated. The installation of the microwave irradiation was therefore successful and experiments with the MCBJ-SET can be carried out in the next step. Although the antenna shows slightly better qualities, I would recommend using the antenna and stripline in the future for redundancy reasons and to avoid the frequency-dependent characteristics of the microwave transmitters.

Various atomic contacts with different distributions of their individual channel transmissions were measured. I discussed a selection of the most interesting examples starting with a tunnel contact that is only showing PAT. Then I presented contacts with increasing transmission, which exhibit a variety of features when exposed to microwaves, which are best represented in color maps. With regard to the microwave effects, all features could be successfully assigned to various known mechanisms. Firstly, there is PAT which can be fully understood within the framework of the TIEN-GORDON model. The measurement results could be reproduced using simulations based on an experimental *IV*-curve in the absence of microwave irradiation and based on a theoretical *IV*-curve which was obtained by fitting the experimental *IV*-curve in order to determine transmissions of the individual channels. This way, the local amplitude respectively the attenuation of the microwaves could be determined as well. In addition, PAMARs were observed, which goes beyond the simple TIEN-GORDON model, as the differences between the measured data and the simulation show.

A closer look at the SHAPIRO steps reveals that they are not correctly described by a BESSEL function as expected from theory, but more appropriately by the square of a BESSEL function. Other work on similar systems has also found this phase-incoherent tunneling of COOPER pairs can be better modeled by a modified version of the TIEN-GORDON equation. It is therefore debatable whether the replicas of the supercurrent should be referred to as SHAPIRO steps. The half-integer SHAPIRO steps, which are not actually SHAPIRO steps after all, would represent a new observation.

Future measurements should focus on the MCBJ-SET experiment, but several things can be learned from my measurements on simple MCBJs. For power-resolved measurements, the distribution of the measuring points should be selected in such a way that a good resolution is achieved for all power levels. Overall, more points should be measured on the power axis and the measurements could be carried out over a longer period of time in order to further improve the measurement results as

the atomic contacts have proven to be very stable. Controlling the temperature is an interesting parameter that has been missing until now. It would be especially interesting to investigate how the half-integer SHAPIRO steps change with the temperature.

Further analysis of the existing measurement data could focus on the correct implementation of the PAMAR and as well as the investigation of the origin of the curved SHAPIRO steps. In addition, the data could be visualized in the SHAPIRO-lobe representation to allow for a better comparison with other publications on fractional SHAPIRO steps.

## 6 Appendix

**Table 6.1:** Summary of the fabrication of a aluminum MCBJ adapted from [56].

Fabrication step	Materials, machines, parameter and procedure
Wafer preparation	Remove plastic foil, glue bronze wafer onto polishing block
Polishing	Use wet sanding paper with increasing grit starting with 600
Cleaning	Acetone, IPA and ultrasonic bath
Preparations	Defrost polyimide, protect spin coater with aluminum foil, cover chuck with parafilm & holes, prepare vacuum oven, preheat convection oven to 135 °C
Drying	Hot plate at 100 °C for 1 min, blow with N <sub>2</sub>
Sacrificial layer	Cover wafer with Durimide 115A, mind air bubbles
Spinning	Spread at 300 rpm for 30 s, spin at 5000 rpm for 90 s, ramps for 3 s (Program 3)
Soft baking	Bake wafer in convection oven at 135 °C for 5 min
Hard baking	400 °C for 30 min
Drying	Hot plate at 100 °C for 1 min, blow with N <sub>2</sub>
Spacing layer	Coat wafer about 90 % with copolymer MMA(8.5)MAA EL11
Spinning	Spread at 500 rpm for 5 s, spin at 2500 rpm for 90 s, ramps for 3 s (Program 1)
Baking	Bake wafer on hot plate at 150 °C for 60 s
Electronic resist	Coat wafer about 90 % with 950 PMMA A4
Spinning	Spread at 500 rpm for 5 s, spin at 5000 rpm for 60 s, ramps for 3 s (Program 2)
Baking	Bake wafer in convection oven at 170 °C for 30 min
Wafer cutting	Clean wafer cutter, use spacers to cut 18 mm × 3 mm
Exposure	Writing sample with high current mode, 10 kV, WD of 5 mm, small and big writing fields and an area dose of 170 µC/cm <sup>2</sup>
Development	Gently move sample a solution of 1:3 MIBK to IPA for 25 s Stop development with 1 min in IPA and blow dry with N <sub>2</sub>
Loading samples	Clean and heat sample holder, load in the evening before Orient the lead contacting the island with a finger from the bottom towards the hook of the sample holder
Shadow evaporation	First layer: 50 nm (S1a/b)) or 80 nm (S2a/b) aluminum at 4° (Second layer: 90 nm aluminum at 40° - S1a/b only)
Lift-off	Put samples in closed vial and on hot plate 60 °C for 1 h Use pipette to flush residues of resists/metal away.
Reactive-ion etching	Isotropic etching with O <sub>2</sub> plasma by enhancing the chemical part through low acceleration voltage, high ICP power, high O <sub>2</sub> flow and pressure and elevated temperature to remove ~ 500 nm Program (MCBJ SSET Unteraetzen v5 @ 100 °C)
Contacting	Connect contact pads to 60 µm Cu cables with conducting silver and fix them with UHU Sofortfest using a toothpick

## 6.1 Microwave Effects on Low-Ohmic Contacts

When we turned on the microwaves for the first time, we observed an almost instantaneous rise in temperature. The increase in temperature is of course dependent on the applied microwave power, but also on the frequency as different microwave frequencies have different transmissions through the cables and exhibit different cavity effects depending on their wavelength.

As one would expect, the increase in temperature weakens superconductivity as shown in figure 6.1 where the same measurement without and with microwaves (10 GHz, -2 dBm) are put side by side. Figure 6.1b shows reduced critical currents and critical magnetic field at a temperature of  $\sim 750$  mK compared to the measurement without microwaves shown in 6.1a which was done at temperatures around 750 mK. The fact that even the measurement without microwaves is far from the base temperature is due to Joule heating caused by the normal conducting state of the sample that is reached once the critical current  $I_{C,2}$  has been exceeded.

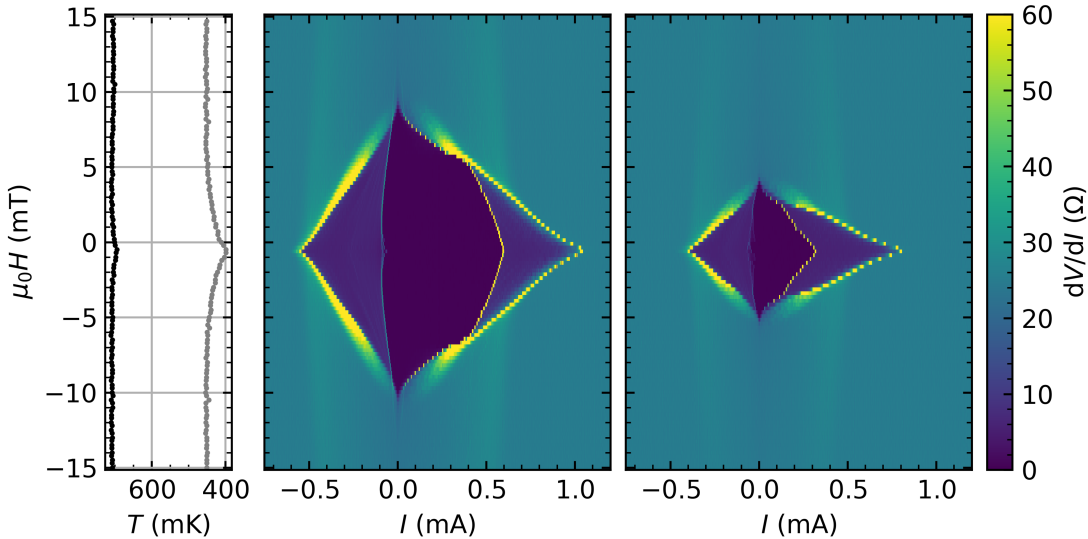


**Figure 6.1:** Magnetic field study comparing sample S2a in the low-Ohmic state (a) without and (b) under microwave irradiation. The microwave irradiation causes significant heating and therefore weakens superconductivity.

## 6.2 Atomic Contacts in Magnetic Field

The magnetic field studies presented here are similar to the measurements for the low-Ohmic contacts. Figure 6.2 shows two contacts of sample S2b with both having a total conductance of approximately  $2G_0$ , that look very different from one another.

Compared to the low-Ohmic contacts from the closed MCBJ, we can see that the hysteresis disappeared once the MCBJ was opened for the first time. The color map is symmetric along the voltage axis, up- and down-sweep look identical. This means we have an overdamped JOSEPHSON junction with a STEWARD-MCCUMBER parameter

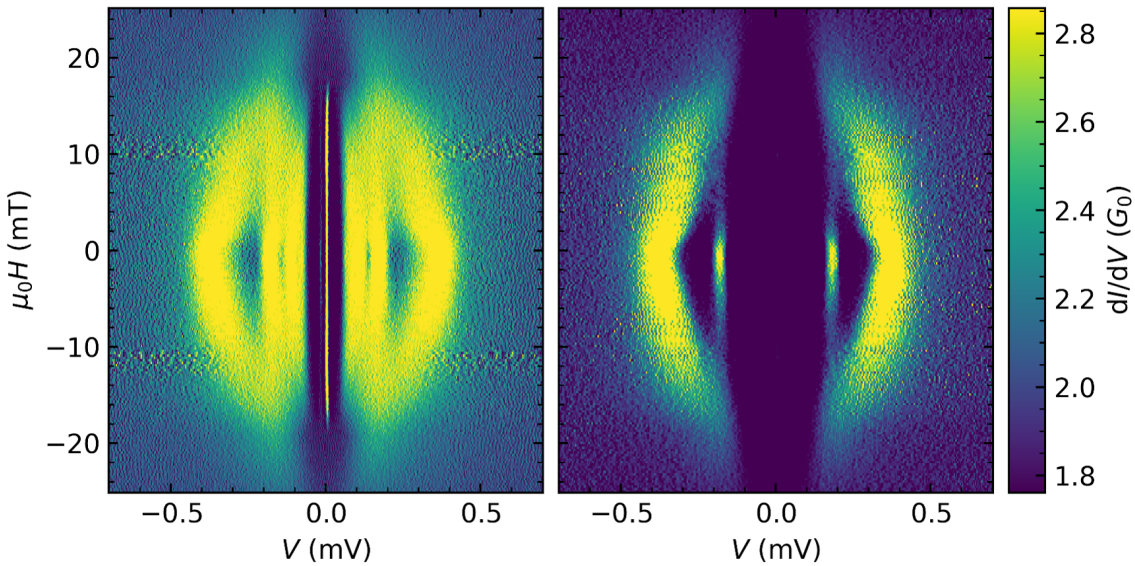


**Figure 6.2:** Magnetic field study for two contacts having a comparable total conductance of  $2 G_0$ . The two contacts shown here are discussed in detail in the chapters 4.2.3 and 4.2.3.

$\beta_C \ll 1$  as defined in equation 2.10. The magnetic field studies performed on sample S1b look similar, the differences that showed up in the low-Ohmic contacts vanish as the opened break-junction becomes the dominating constriction.

Other than for the color maps for the low-Ohmic contacts in the previous chapter where we plotted the differential resistance over a current axis, we now plot the differential conductance normalized by the conductance quantum  $G_0$  over a voltage axis that has been normalized to the gap energy  $\Delta$  as these are the natural units for atomic contacts. The applied magnetic field is still plotted on the y-axis. The temperature throughout the measurement on high-Ohmic contacts without microwaves is very constant and with  $T \approx 40$  mK significantly lower than for the low-Ohmic contacts as the currents passing through the junction are significantly lower as well.

Even if  $2.09 G_0$  and  $1.97 G_0$  are very comparable conductances, the figures 6.2a and 6.2b still look very different. The overall shape, meaning for voltages  $V > 2\Delta/e$  and for high magnetic fields, is similar. For small magnetic fields, however, the contact in figure 6.2a shows a strong supercurrent and MAR up to the order  $m = 3$  below the voltage of  $V = 2\Delta/e$ . Figure 6.2b, on the other hand, only shows remainders of Andreev reflection at  $V = \Delta/e$ . Already from this, one can tell, that the contact in 6.2a has to have a higher leading transmission than 6.2b. A more detailed analysis of the individual sets of transmissions is presented in the subchapters corresponding to the contacts.

### 6.3 Simulation based on a theoretical curve

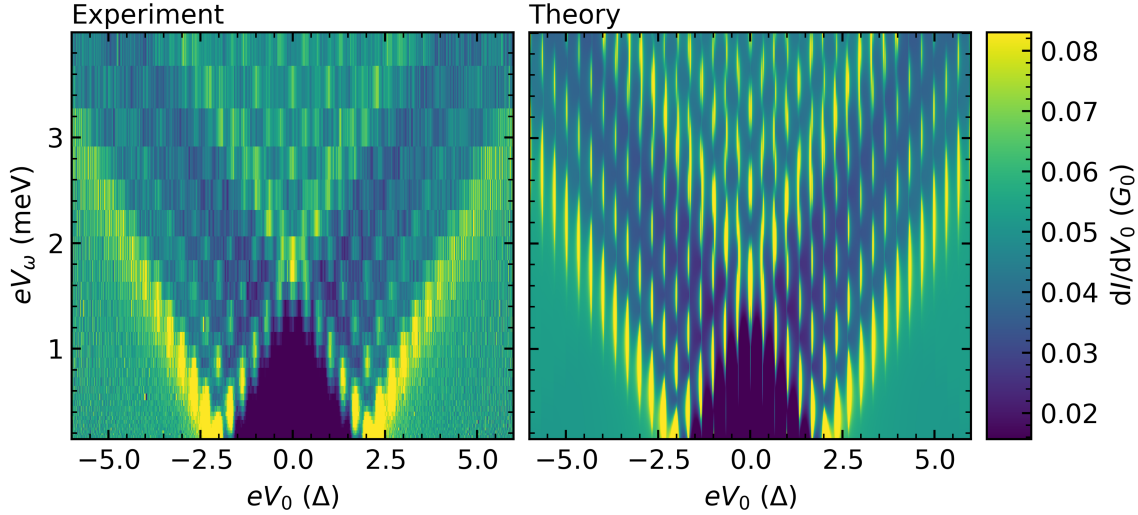


**Figure 6.3:** Power study comparing the experimental data with a simulation based on a theoretical  $dI/dV$ -curve in the absence of microwave irradiation obtained from a fit of the transmission channels. The transmission of the contact is  $\tau = 0.05$ ,  $G = 0.05 G_0$ . The microwaves have been coupled in via the stripline and their frequency was fixed to  $\nu = 15$  GHz. From minimizing the MSD of the two maps we find for the damping parameter  $\gamma = \frac{V_\omega}{V_{\text{out}}} = 0.0146$ . The simulation using the theory curve produces much sharper features than for the measured one, but otherwise shows the same pattern.

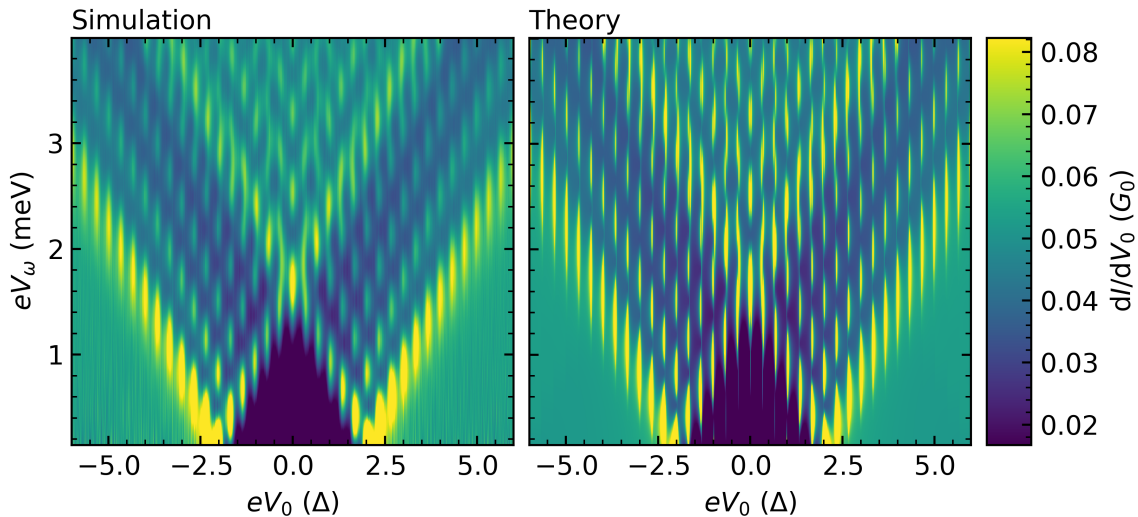


**Figure 6.4:** Power study comparing the two simulations based on a measured  $dI/dV$ -curve without microwave irradiation and based on a theoretical  $dI/dV$ -curve in the absence of microwave irradiation obtained from a fit of the transmission channels. All parameters are identical to figures 4.11 and 6.3. This comparison clearly shows the effect of thermal rounding on the experimental data.

## References

1. Averin, D. V. & Likharev, K. K. Coulomb blockade of single-electron tunneling, and coherent oscillations in small tunnel junctions. *Journal of Low Temperature Physics* **62**, 345–373 (1986).
2. Jezouin, S., Iftikhar, Z., Anthore, A., Parmentier, F. D., Gennser, U., Cavanna, A., Ouerghi, A., Levkivskyi, I. P., Idrisov, E., Sukhorukov, E. V., Glazman, L. I. & Pierre, F. Controlling charge quantization with quantum fluctuations. *Nature* **536**, 58–62 (2016).
3. Lorenz, T., Sprenger, S. & Scheer, E. Coulomb Blockade and Multiple Andreev Reflection in a Superconducting Single-Electron Transistor. *Journal of Low Temperature Physics* **191**, 301–315 (2018).
4. Sobral Rey, L. *Interplay between charging effects and multiparticle charge transport processes in a tunable single electron transistor* (Universität Konstanz, Konstanz, 2022).
5. Sobral Rey, L., Ohnmacht, D. C., Winkelmann, C. B., Siewert, J., Belzig, W. & Scheer, E. Interplay of Andreev Reflection and Coulomb Blockade in Hybrid Superconducting Single-Electron Transistors. *Physical Review Letters* **132**, 057001 (2024).
6. Sprenger, S. *Interplay between charging effects and multi-particle transport in superconducting single electron transistors with tunable junctions* (Universität Konstanz, Konstanz, 2019).
7. Tinkham, M. *Introduction to Superconductivity* (McGraw Hill, 1996).
8. Meservey, R. & Tedrow, P. M. Properties of Very Thin Aluminum Films. *Journal of Applied Physics* **42**, 51–53 (1971).
9. Arutyunov, K. Y., Sedov, E. A., Zavialov, V. V., Stavrinidis, A., Stavrinidis, G., Chatzopoulos, Z., Adikimenakis, A., Konstantinidis, G., Florini, N., Chatzopoulou, P., Kehagias, T., Dimitrakopoulos, G. P. & Komninou, P. The Critical Temperature of Superconducting Aluminum Films. *Physics of Metals and Metallography* **124**, 53–57 (2023).
10. Giaever, I. Energy Gap in Superconductors Measured by Electron Tunneling. *Physical Review Letters* **5**, 147–148 (1960).
11. Landauer, R. Electrical resistance of disordered one-dimensional lattices. *The Philosophical Magazine: A Journal of Theoretical Experimental and Applied Physics* **21**, 863–867 (1970).
12. Schirm, C. *Einfluss hoher Ströme auf atomare Kontakte* (Universität Konstanz, Konstanz, 2009).
13. Scheer, E., Joyez, P., Esteve, D., Urbina, C. & Devoret, M. H. Conduction Channel Transmissions of Atomic-Size Aluminum Contacts. *Physical Review Letters* **78**, 3535–3538 (1997).

14. Cuevas, J. C., Martín-Rodero, A. & Yeyati, A. L. Hamiltonian approach to the transport properties of superconducting quantum point contacts. *Physical Review B* **54**, 7366–7379 (1996).
15. Agrait, N., Yeyati, A. L. & van Ruitenbeek, J. M. Quantum properties of atomic-sized conductors. *Physics Reports* **377**, 81–279 (2003).
16. Josephson, B. D. Possible new effects in superconductive tunnelling. *Physics Letters* **1**, 251–253 (1962).
17. Barone, A. & Paternò, G. *Physics and Applications of the Josephson Effect* in (Wiley, 1982).
18. Gross, R. & Marx, A. *Applied Superconductivity: Josephson Effect and Superconducting Electronics* Walther-Meißner-Institut, 2005.
19. Helbig, W. in *Praxiswissen in der Messtechnik: Arbeitsbuch für Techniker, Ingenieure und Studenten* (ed Helbig, W.) 25–39 (Springer Fachmedien, Wiesbaden, 2021).
20. Stewart, W. C. CURRENT-VOLTAGE CHARACTERISTICS OF JOSEPHSON JUNCTIONS. *Applied Physics Letters* **12**, 277–280 (1968).
21. McCumber, D. E. Structures for the Measurement of High-Frequency Properties of Point-Contact Josephson Junctions. *Journal of Applied Physics* **39**, 297–306 (1968).
22. Cron, R. *Les contacts atomiques : un banc d'essai pour la physique mésoscopique* (Université Pierre et Marie Curie - Paris VI, 2001).
23. Waldram, J. R. *Superconductivity of Metals and Cuprates* (CRC Press, Boca Raton, 1996).
24. Russer, P. Influence of Microwave Radiation on Current-Voltage Characteristic of Superconducting Weak Links. *Journal of Applied Physics* **43**, 2008–2010 (1972).
25. Gregers-Hansen, P. E. & Levinsen, M. T. Normal-State Resistance as the Determining Parameter in the Behavior of Dayem Bridges with Sinusoidal Current-Phase Relations. *Physical Review Letters* **27**, 847–849 (1971).
26. Hamilton, C. A. Josephson voltage standards. *Review of Scientific Instruments* **71**, 3611–3623 (2000).
27. Tien, P. K. & Gordon, J. P. Multiphoton Process Observed in the Interaction of Microwave Fields with the Tunneling between Superconductor Films. *Physical Review* **129**, 647–651 (1963).
28. Dayem, A. H. & Martin, R. J. Quantum Interaction of Microwave Radiation with Tunneling Between Superconductors. *Physical Review Letters* **8**, 246–248 (1962).
29. Cuevas, J. C. & Scheer, E. *Molecular Electronics* (WORLD SCIENTIFIC, 2010).

30. Kot, P., Drost, R., Uhl, M., Ankerhold, J., Cuevas, J. C. & Ast, C. R. Microwave-assisted tunneling and interference effects in superconducting junctions under fast driving signals. *Physical Review B* **101**, 134507 (2020).
31. Danchi, W. C., Habbal, F. & Tinkham, M. ac Josephson effect in small-area superconducting tunnel junctions at 604 GHz. *Applied Physics Letters* **41**, 883–885 (1982).
32. Gregers-Hansen, P. E., Hendricks, E., Levinse, M. T. & Pickett, G. R. Subharmonic Energy-Gap Structure and a Josephson-Radiation-Enhanced Gap in Dayem Bridges. *Physical Review Letters* **31**, 524–527 (1973).
33. Cuevas, J. C., Martín-Rodero, A. & Yeyati, A. L. Shot Noise and Coherent Multiple Charge Transfer in Superconducting Quantum Point Contacts. *Physical Review Letters* **82**, 4086–4089 (1999).
34. Cron, R., Goffman, M. F., Esteve, D. & Urbina, C. Multiple-Charge-Quanta Shot Noise in Superconducting Atomic Contacts. *Physical Review Letters* **86**, 4104–4107 (2001).
35. Soerensen, O. H., Kofoed, B., Pedersen, N. F. & Shapiro, S. Microwave dependence of subharmonic gap structure in superconducting junctions. *Physical Review B* **9**, 3746–3756 (1974).
36. Cuevas, J. C., Heurich, J., Martín-Rodero, A., Levy Yeyati, A. & Schön, G. Subharmonic Shapiro Steps and Assisted Tunneling in Superconducting Point Contacts. *Physical Review Letters* **88**, 157001 (2002).
37. Zimmermann, U. & Keck, K. Multiple Andreev-reflection in superconducting weak-links in the interaction with external microwave-fields. *Zeitschrift für Physik B Condensed Matter* **101**, 555–560 (1996).
38. Chauvin, M. *The Josephson Effect in Atomic Contacts* (Université Pierre et Marie Curie - Paris VI, 2005).
39. Chauvin, M., Vom Stein, P., Pothier, H., Joyez, P., Huber, M. E., Esteve, D. & Urbina, C. Superconducting Atomic Contacts under Microwave Irradiation. *Physical Review Letters* **97**, 067006 (2006).
40. Peters, O., Bogdanoff, N., Acero González, S., Melischek, L., Simon, J. R., Reecht, G., Winkelmann, C. B., von Oppen, F. & Franke, K. J. Resonant Andreev reflections probed by photon-assisted tunnelling at the atomic scale. *Nature Physics* **16**, 1222–1226 (2020).
41. Siebrecht, J., Huang, H., Kot, P., Drost, R., Padurariu, C., Kubala, B., Ankerhold, J., Cuevas, J. C. & Ast, C. R. Microwave excitation of atomic scale superconducting bound states. *Nature Communications* **14**, 6794 (2023).
42. Haxell, D. Z., Coraiola, M., Sabonis, D., Hinderling, M., ten Kate, S. C., Cheah, E., Krizek, F., Schott, R., Wegscheider, W., Belzig, W., Cuevas, J. C. & Nichele, F. Microwave-induced conductance replicas in hybrid Josephson junctions without Floquet—Andreev states. *Nature Communications* **14**, 6798 (2023).

43. Carrad, D. J., Stampfer, L., Olsteins, D., Petersen, C. E. N., Khan, S. A., Krogstrup, P. & Jespersen, T. S. Photon-Assisted Tunneling of High-Order Multiple Andreev Reflections in Epitaxial Nanowire Josephson Junctions. *Nano Letters* **22**, 6262–6267 (2022).
44. Falci, G., Bubanja, V. & Schön, G. Quasiparticle and Cooper pair tunneling in small capacitance Josephson junctions. *Zeitschrift für Physik B Condensed Matter* **85**, 451–458 (1991).
45. Roychowdhury, A., Dreyer, M., Anderson, J., Lobb, C. & Wellstood, F. Microwave Photon-Assisted Incoherent Cooper-Pair Tunneling in a Josephson STM. *Physical Review Applied* **4**, 034011 (2015).
46. Devoret, M. H., Esteve, D., Grabert, H., Ingold, G.-L., Pothier, H. & Urbina, C. Effect of the electromagnetic environment on the Coulomb blockade in ultrasmall tunnel junctions. *Physical Review Letters* **64**, 1824–1827 (1990).
47. Dayem, A. H. & Wiegand, J. J. Behavior of Thin-Film Superconducting Bridges in a Microwave Field. *Physical Review* **155**, 419–428 (1967).
48. Panghotra, R., Raes, B., de Souza Silva, C. C., Cools, I., Keijers, W., Scheerder, J. E., Moshchalkov, V. V. & Van de Vondel, J. Giant fractional Shapiro steps in anisotropic Josephson junction arrays. *Communications Physics* **3**, 1–8 (2020).
49. Raes, B., Tubbsrinuan, N., Sreedhar, R., Guala, D. S., Panghotra, R., Dausy, H., De Souza Silva, C. C. & Van De Vondel, J. Fractional Shapiro steps in resistively shunted Josephson junctions as a fingerprint of a skewed current-phase relationship. *Physical Review B* **102**, 054507 (2020).
50. Snyder, R., Trimble, C., Rong, C., Folkes, P., Taylor, P. & Williams, J. Weak-link Josephson Junctions Made from Topological Crystalline Insulators. *Physical Review Letters* **121**, 097701 (2018).
51. Trimble, C. J., Wei, M. T., Yuan, N. F. Q., Kalantre, S. S., Liu, P., Han, H.-J., Han, M.-G., Zhu, Y., Cha, J. J., Fu, L. & Williams, J. R. Josephson detection of time-reversal symmetry broken superconductivity in SnTe nanowires. *npj Quantum Materials* **6**, 1–6 (2021).
52. Iorio, A., Crippa, A., Turini, B., Salimian, S., Carrega, M., Chiroli, L., Zanvier, V., Sorba, L., Strambini, E., Giazotto, F. & Heun, S. Half-integer Shapiro steps in highly transmissive InSb nanoflag Josephson junctions. *Physical Review Research* **5**, 033015 (2023).
53. Prestel, M. *Magnetic Order in Atomic Contacts of Strong Paramagnets* (Universität Konstanz, Konstanz, 2020).
54. Janvier, C., Tosi, L., Girit, C. O., Goffman, M. F., Pothier, H. & Urbina, C. Superconducting atomic contacts inductively coupled to a microwave resonator. *Journal of Physics: Condensed Matter* **26**, 474208 (2014).
55. Bretheau, L. *Localized Excitations in Superconducting Atomic Contacts: PROBING THE ANDREEV DOUBLET* (Ecole Polytechnique X, 2013).

56. Raif, P. *Fabrication of a Superconducting Single-Electron Transistor* (Universität Konstanz, Konstanz, 2023).
57. Duprat, R. & Yeyati, A. L. Phase diffusion and fractional Shapiro steps in superconducting quantum point contacts. *Physical Review B* **71**, 054510 (2005).



## Acknowledgments

At the end of this master's thesis I would like to thank several people in different ways. First of all, I would like to thank my supervisor Prof. Dr. Elke Scheer for her excellent supervision. I always found the weekly MesoSupra meetings very helpful and was able to learn a lot. I highly appreciate her expertise in this broad field of mesoscopic physics. Whenever a known problem arises, Prof. Scheer immediately knows which of her students has already written about it in his thesis. Furthermore, Prof. Scheer is an excellent proofreader, her corrections are always prompt and she finds every little mistake. All in all, I would just like to say thank you for the opportunity to do my master's thesis in this group. Thank you, Elke, also for supervising my bachelor's thesis, which I did in Grenoble and for which I missed the opportunity to write an acknowledgment. I would like to thank you for allowing me to attend the SFB conference in Irsee, which is not a matter of course.

Next, I would like to thank Oliver Irtenkauf, who supervised me on a daily basis during my master's thesis. Working with you, Olli, was a pleasure at all times. The work in the lab was always more fun when you were there. You were always available for me and you were always able to help me, especially with my programming problems. I would also like to thank Ronja, who has always motivated me to tackle even the most unpleasant tasks. Then, I would like to thank all my office colleagues and those who came to the office to visit us regularly. Overall, I would like to thank all the members of AG Scheer for the great time I was able to spend with you during my master's thesis. I will always look back on our lunch and cake breaks, and joint activities with delight.

Further thanks are due to Prof. Cuevas for the helpful discussions on the theory of my project and to the SFB, which organizes many great events such as the pizza seminar.

Since my time as a student ends with my master's degree, I would like to thank all my great fellow students for the last five years. Special thanks go to Franz, with whom I worked on almost all the exercise sheets together, and Andrea, who has not always had an easy time with me as her lab partner. I think she was never even able to read my parts of the lab report, because I always delivered them just before the deadline.

Last but not least, I would like to thank my family, who always believed in me. I would like to thank my sisters for always being there for me, as well as my parents, and also for their financial support. It was always a pleasure to come home to you at the weekends.